Aging Pathobiology and Therapeutics 2026; 8(3): xx-xx *xx*
DOI: 10.31491/APT.2023.03.105

RESEARCH

Deciphering the action of indole analogues on selected targets for neuroprotection in Alzheimer's disease: network pharmacology, *in silico*, and *in vitro* approaches

Manas Kumar Gedla[a], Ramanathan Muthiah[a, *]

[a] *Department of Pharmacology, PSG College of Pharmacy, Coimbatore-641 004, Tamil Nadu, India.*

Abstract

Alzheimer's disease is the leading cause of cognitive decline worldwide, and the lack of truly effective disease-modifying treatments has increased interest in phytochemical-derived molecules as alternative therapeutic options for AD. This study combined network pharmacology, molecular docking, molecular dynamics simulations, and *in vitro* experimental validation to evaluate a series of indole-based analogs as potential candidates for treating Alzheimer's disease. Protein–protein interaction networks centered on Alzheimer's-related targets were constructed using STRING, Cytoscape 3.10.2, and DAVID, while Gene Ontology and Kyoto Encyclopedia of Genes and Genomes pathway analyses helped identify the key biological processes, cellular components, and molecular functions involved in disease progression. The binding affinities between the indole analogs and target proteins were assessed through molecular docking using MolSoft ICM Pro, which also handled protein and ligand preparation, complemented by predictions of ADME/T properties and blood–brain barrier permeability. The most effective compounds were subjected to molecular dynamics simulations using CHARMM-GUI and NAMD software to evaluate the stability of each protein–ligand complex over time. For biological validation, five indole-based analogs were tested at multiple concentrations in N2a neuroblastoma cells using MTT assays alongside a hypoxia cell model to determine IC_{50} values. Among the tested compounds, A13 emerged as the primary lead compound, demonstrating favorable molecular docking, stable molecular dynamics behavior, negative molecular mechanics/generalized born surface area (MM/GBSA) binding free energy, acceptable ADMET properties, predicted blood–brain barrier permeability, and significant neuroprotective activity. When challenged with glutamate-induced toxicity, A13 and A33 returned IC_{50} values of 1.87 and 2.28 μM, respectively. Western blot analysis verified that both compounds promoted GSK3β phosphorylation, indicating a meaningful therapeutic mechanism. By combining computational and experimental strategies, this study identified A13 as potential GSK3β inhibitors, supported by robust structural and cell viability evidence that warrants their continued development as therapeutic candidates for Alzheimer's disease.

Keywords: Alzheimer's disease, indole analogs, network pharmacology, molecular docking, molecular dynamics simulation

Introduction

Alzheimer's disease (AD) is an irreversible and progressive neurological disorder and a leading cause of dementia-related death worldwide. The mortality rate due to AD and other dementias has increased steadily over the past few decades. Despite extensive research, current therapies remain largely symptomatic and fail to halt or reverse disease progression. The major pathological features of AD include amyloid-β plaque accumulation, tau hyperphosphorylation, synaptic dysfunction, neuroinflammation, and neuronal loss. Although many molecular targets have been studied, translating experimental findings into clinical treatments has been unsuccessful, highlighting critical research gaps. These gaps are attributable to the multifactorial nature of AD, poor blood-brain barrier permeability, single-target drug strategies, and unpredictable toxicity

* Corresponding author: Ramanathan Muthiah
Mailing address: Department of Pharmacology, PSG College of Pharmacy, Peelamedu, Coimbatore, 641004, Tamil Nadu, India.
Email: ramanathanm@psgpharma.ac.in
Received: 08 June 2026 / Revised: 08 July 2026
Accepted: 10 August 2026 / Published: 30 September 2026

profiles. Therefore, it is imperative to identify safe, brain-penetrating, multitarget, and pathway-oriented therapeutic agents using innovative and integrative drug discovery approaches [1, 2]. GSK3β, or glycogen synthase kinase-3 beta, is a versatile serine/threonine protein kinase that regulates several essential cellular processes, including glycogen metabolism, cell cycle progression, apoptosis, gene expression, and neuronal function. It phosphorylates serine and threonine residues on target proteins and is encoded by the GSK3β gene.GSK3β participates in multiple signaling pathways, notably the Wnt pathway, which controls differentiation, proliferation, and cell fate, and the insulin signaling pathway, where it inhibits glycogen synthase to regulate glycogen synthesis. Its activity is tightly controlled by phosphorylation, protein–protein interactions, and sub-cellular localization [3]. Phosphorylation at serine 9 (Ser9) inhibits GSK3β activity, whereas phosphorylation at other regulatory sites activates the enzyme. Dysregulation of GSK3β has been implicated in several diseases, including diabetes, cancer, bipolar disorder, Alzheimer's disease, and other neurodegenerative disorders [4]. GSK3β also suppresses autophagy, and inhibition of this enzyme has been shown to reduce the pathogenesis of Alzheimer's disease by promoting autophagy [5, 6].

Numerous synthetic and natural scaffolds, such as triazoles, indoles, pyrazinamides, aminopyrimidines, benzimidazoles, indirubins, oxadiazoles, thiazoles, hydantoins, paullones, and maleimides, have been explored as ATP-competitive inhibitors, highlighting the importance of nitrogen-containing heterocycles [7]. Despite significant progress, the clinical application of GSK3β inhibitors remains limited due to complex disease relationships, difficulty in defining optimal dosing, and variable therapeutic efficacy [8, 9]. Signal transducer and activator of transcription 3 (STAT3) may also play a role in regulating synaptic plasticity, cell death, and cognitive processes. Human tau-N368 accumulation reduces STAT3 activity by preventing its translocation into the nucleus, as demonstrated by luciferase reporter assays, electrophoretic mobility shift tests, western blotting, and immunofluorescence. STAT3 overexpression decreased neuronal death and corrected tau-N368-induced synaptic impairments. Thus, the development of neuritic plaques and production of amyloid β (Aβ) are significantly influenced by STAT3 activity. The STAT3 pathway controls the biological activity of hippocampal neurons, astrocytes, and microglia, all of which play a major role in the development of AD. In animal studies, tau-induced cognitive deficits were mitigated by activating STAT3, which raised NMDA receptor levels, lowered Bcl-2 levels, and reversed synaptic damage and neuronal death [2, 9-12].

The vast family of structurally related zinc-dependent proteases, known as matrix metalloproteinases (MMPs), specifically matrix metalloproteinase (MMP-2), aids in the control of neural network remodeling, neuron-glial cell communication, neuroimmune response, BBB function, neuronal activity, survival, and death. Neuronal cells express MMP-2, which is less affected by harmful stimuli. When older adult patients develop modest cognitive impairment, their MMP-2 levels also increase. The significant increase in tau levels is closely associated with an increase in MMP-2 levels. MMP-2 showed a strong association with all measured MMPs and TIMPs, as indicated by the Pearson's correlation matrix of CSF biomarkers.

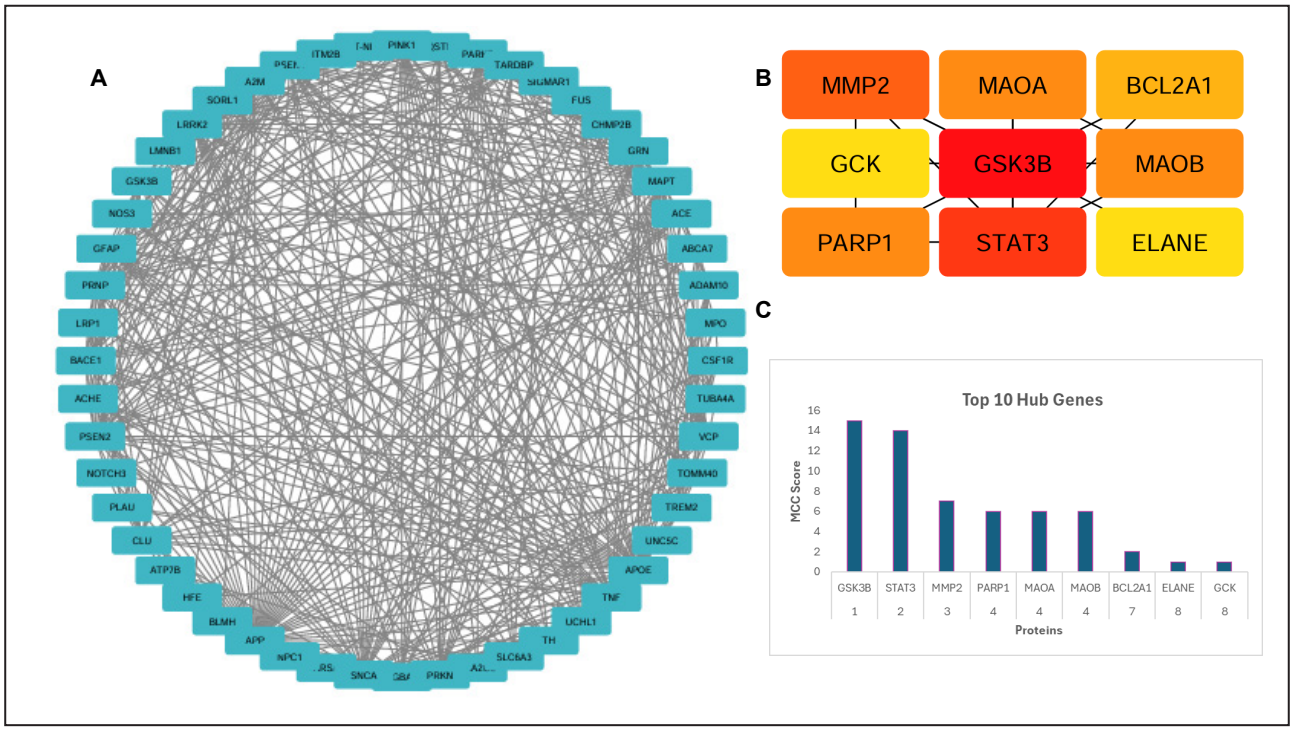

Figure 1. Identification and topological analysis of shared hub targets between indole analogues and Alzheimer's disease network. **(A)** Analysis of the top Hub genes complex biological and molecular interaction. **(B)** Centrality category ranking of GSK3β. **(C)** Maximum Clique Centrality (MCC) algorithm ranking.

Aβ deposits are cleared by MMP-2's direct degradation of Aβ. Conversely, brain parenchymal deterioration may be facilitated by Aβ-induced MMP-2. MMP-2 causes BBB breakdown, and TIMP-2 may counteract this effect. In AD, MMP-2 disrupts oxidative homeostasis [10-14]. Network pharmacology analysis revealed multiple targets of the five hub genes (GSK3β, STAT3, MMP2, PARP1, and MAOB). The selection of GSK3β, STAT3, and MMP2 for molecular docking was guided by three criteria: (A) availability of high-resolution co-crystallized structures suitable for structure-based docking; (B) Protein–protein interaction (PPI) network centrality scores (GSK3β ranked first, STAT3 second, and MMP2 third by MCC); and (C) direct mechanistic relevance to the core pathological features of Alzheimer's disease: tau hyperphosphorylation (GSK3β), neuroinflammatory signaling (STAT3), and BBB disruption (MMP2). PARP1, identified as a hub gene, is primarily associated with DNA damage repair and oxidative stress rather than AD-specific pathological cascades, and high-quality ligand-bound crystal structures were not available at the time of the study. MAOB ranked fifth and was most relevant to monoamine metabolism, which is tangential to the mechanism of the indole scaffold. Indoles have been widely investigated as potential GSK3β inhibitors for treating Alzheimer's disease. However, previous investigations have predominantly focused on classical indole-derived scaffolds, including indirubins, paullones, and maleimide derivatives, and their derivatives. In contrast, the present study evaluated a structurally distinct series of synthetic indole analogs bearing strategically substituted aromatic and heterocyclic moieties designed to improve target recognition and neuroprotective efficacy. To the best of our knowledge, these compounds have not been investigated using an integrated workflow combining network pharmacology, molecular docking, molecular dynamics (MD) simulations, ADMET prediction, and experimental validation for Alzheimer's disease.

Materials and methods

Network pharmacology

Web-based study mining and network construction, as well as Cytoscape and STRING PPI network construction were performed on a Windows 10 system with an Intel Core™ i3-8130U CPU @ 2.20 GHz, 16.00 GB RAM, a 64-bit operating system, and x64-based processor. AD-related genes were obtained from GeneCards using the keyword "Alzheimer's disease," retrieving 5,260 genes. Genes with a relevance score > 60 were selected for subsequent protein–protein interaction analysis [15, 16]. Target genes were submitted to the STRING 12.0 database (https://string-db.org/) using the "Homo sapiens" setting, with the confidence threshold of > 0.9 [17, 18]. The compound-target network was constructed and visualized using Cytoscape v_3.7.1 [19]. Gene Ontology (GO) and Kyoto Encyclopedia of Genes and Genomes (KEGG) pathway annotation were performed using the ClueGO plug-in in Cytoscape, with significance threshold of adjusted *P*-value < 0.05 [20, 21].

Virtual screening

Ligand libraries prepared from the Drug Bank (> 5000) and in-house compound database were screened against

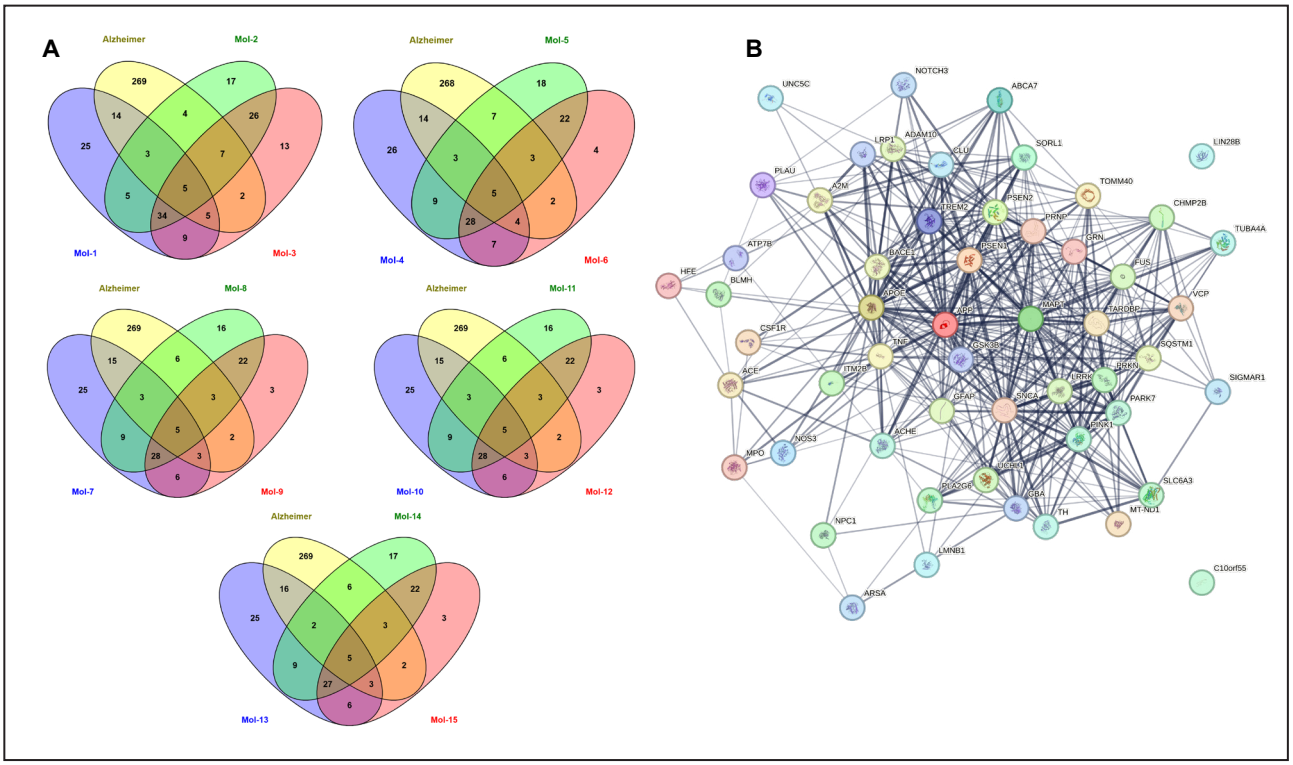

Figure 2. Network analysis of potential therapeutic targets and protein-protein interactions in Alzheimer's disease. **(A)** Target relevant to the treatment of Alzheimer's. **(B)** protein-protein interaction related to Alzheimer's disease.

GSK3β, STAT3, and MMP2 using high-throughput molecular docking with Molsoft ICM-Pro software. The top 10% of hits were further docked with extra precision, and ADMET and pharmacokinetic features were evaluated. Based on molecular interactions, 14 ligands were selected for further refinement using MD simulations and *in vitro* studies.

Ligand preparation

The structures of the synthetic compounds were obtained from the institution, converted into 2D drawings, and processed using ICM. The formal charge of each atom was calculated using the ICM pKa prediction model at a pH of 7. Stereochemistry and hydrogen atoms were assigned accordingly. Each atom was assigned an MMFF94 forcefield atom type and a partial charge. The 2D ligand was then converted to 3D, rotational bonds were sampled, and all atoms were minimized in the Cartesian coordinates in the absence of the receptor maps as the starting ligand conformation for docking [16, 22].

Molecular docking

Compounds were docked against GSK3β (PDB: 6Y9R), STAT3 (PDB: 6NJS), and MMP2 (PSB: 7XJO) using Molsoft ICM-Pro software. Protein structures were prepared by removing water molecules, acetate, and glycerol. A13×18×20 grid was generated around the ATP-binding site of GSK3β. Compounds were imported as SDF files and docked; 2D and 3D interaction poses were visualized in Molsoft ICM Pro [23, 24].

Drug likeness and ADME/T predictions

The ADMET Parameters and pharmacokinetic characteristics of selected compounds were estimated using the Molsoft ICM Pro database. Seven of the 14 molecules showing BBB clearance and the best docking scores (DLID score of > −32) were carried forward for full ADMET profiling [25-27].

Toxicity parameters

Compounds were screened for PAINS flags using Molsoft ICM Pro to identify and exclude potential false-positive hits. Predicted hERG channel binding and inhibition were assessed using Molsoft ICM Pro to evaluate cardiac safety risk. Compounds were evaluated as P-gp substrates or inhibitors using Molsoft ICM Pro to assess BBB penetration potential. QSAR-based pro-inflammatory potential was estimated for each compound using Molsoft ICM Pro. Acute oral toxicity (LD_{50}) was predicted *in silico* using QSAR models in MolSoft ICM-Pro, based on molecular descriptors and structural alerts.

MD simulation

Ligand topology files were generated using the CHARMM-GUI web portal and advanced MD simulations in the NAMD software [28]. The system was solvated in an aqueous solution containing potassium and chloride ions to achieve charge neutrality [29, 30]. Energy minimization was performed using the steepest descent algorithm for 1,000 steps. Equilibration was performed for 100 ps in the NVT ensemble, followed by 100 ps in

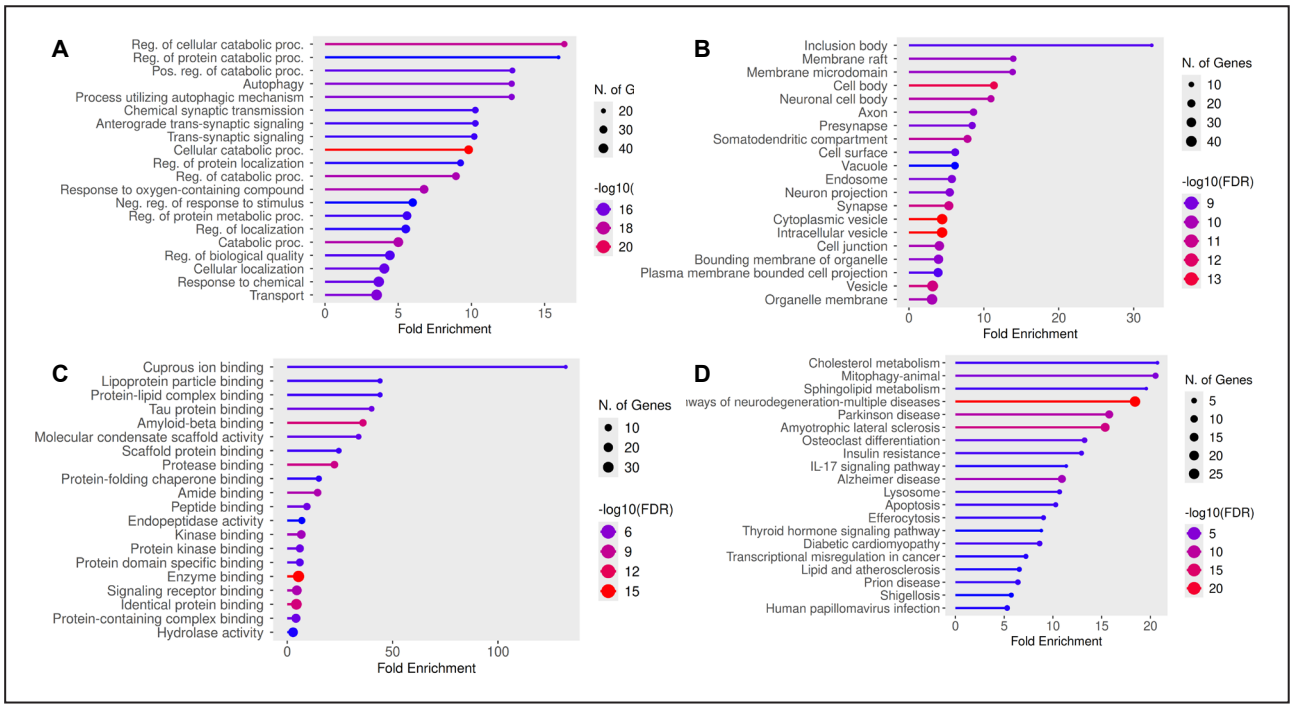

Figure 3. Functional annotation and pathway enrichment analysis of the shared hub targets. **(A)** Gene Ontology (GO) biological process enrichment analysis showing the significantly enriched biological processes. **(B)** GO cellular component enrichment analysis depicting the cellular compartments associated with the target genes. **(C)** GO molecular function enrichment analysis highlighting the molecular functions of the identified targets. **(D)** Kyoto Encyclopedia of Genes and Genomes (KEGG) pathway enrichment analysis showing the major pathways associated with the target genes. The x-axis represents fold enrichment, while dot size indicates the number of associated genes and dot color represents the −log10 (FDR), with higher values indicating greater statistical significance.

the NPT ensemble at 300 K and 1 bar. The production MD simulation was performed for 100 ns under NPT conditions. The initial 10 ns of each trajectory was excluded as the equilibration phase; Root mean square deviation (RMSD), root mean square fluctuation (RMSF), radius of gyration (Rg), solvent-accessible surface area (SASA), and hydrogen bond analyses were performed on the remaining 90 ns of the production trajectory. Each protein–ligand complex was subjected to a single independent 100 ns simulation [31].

In-vitro analysis

MTT assay

Cell viability was assessed using the MTT assay in N2a cells. The drug molecules used were prepared in-house and are listed in Table 1 [32]. A concentration range of 0.25–30 µM was selected based on preliminary cytotoxicity screening. MTT reagent (20 µL) was added to each well and incubated for 4 h; wells were then gently emptied without disturbing the formazan crystals, and 100 µL of DMSO was added to each well and incubated for 15 min. Absorbance was measured at 570 nm. The IC_{50} values were determined from normalized concentration–response curves generated by nonlinear regression using a four-parameter logistic (variable-slope) model in GraphPad Prism version 10.0.1 (GraphPad Software, San Diego, CA, USA). All experiments were performed in three independent biological replicates [33].

Hypoxia-induced cell model

N2a cells seeded in 96-well plates were allowed to adhere overnight in an incubator. Then cultured 96-well plates were then placed in sealed hypoxic chambers flushed with the premixed hypoxic gas at a high flow rate for 5–7 minutes to displace ambient air. N2a cells were exposed to hypoxic conditions for 6 h to establish a hypoxic injury model. The culture medium was replaced with fresh medium containing the respective concentrations of the test or reference compounds at 0.25, 0.5, 1, 3, 10, and 30 µM, and the cells were incubated for an additional 24 h. Cell viability was assessed by the MTT assay as described in the above section [34-37].

Neuroprotective efficacy was calculated as:

$$\text{Neuroprotective efficacy (\%)} = [(ODt_{reatment} - OD_{injury})/(OD_{control} - OD_{injury})] \times 100$$

Glutamate-induced cytotoxicity (GIC)

N2a cells were exposed to 10 mM glutamate for 6 h to induce neuronal injury. The glutamate-containing medium was then replaced with fresh medium containing the respective test compounds or reference drug (AR-A014418) at six concentrations (0.25, 0.5, 1, 3, 10, and 30 µM). The experimental design comprised: (i) untreated normal control, (ii) glutamate-only injury control, (iii) reference drug-treated control (AR-A014418), and (iv) individual treatment groups receiving the synthesized indole analogs. The glutamate-only group served as the disease control for calculating the neuroprotective efficacy [38].

Western blotting

Cells cultured in T25 flasks were induced with 1 µM and 3 µM of drugs A13 and A33, respectively for 24 h. Cells were first washed once with ice-cold HBSS (4 °C) and

Table 1. Molecular docking data of the synthesized compounds with GSK3β (PDB 6Y9R).

Compound	Docking Score (kcal/mol)	H-bond	Hydrophobicity	vdW	Amino acid	Interaction type
A21	−18.41	−1.34	−5.54	−24.65	Val135	H-bond
A13	−18.57	−0.80	−5.84	−25.38	Val135	H-bond
A20	−20.59	−2.13	−5.80	−24.03	Val135	H-bond
A17	−20.19	−2.14	−5.78	−24.19	Val135	H-bond
A18	−22.54	−3.01	−6.00	−25.90	Val135	H-bond
A39	−23.02	−1.90	−5.07	−28.08	Val135	H-bond
A40	−20.86	−2.14	−5.22	−25.96	Val135	H-bond
A34	−19.80	−1.54	−5.67	−24.82	Val135	H-bond
A31	−17.89	0	−6.02	−26.02	Val135	H-bond
A33	−16.93	0	−6.08	−25.18	Phe67	Pi-cation
A32	−16.08	0	−6.18	−24.76	Val135	H-bond
A35	−23.47	−3.33	−6.14	−25.80	Val135	H-bond
A36	−24.47	−2.33	−5.22	−27.36	Val135	H-bond
A72	−18.12	−2.04	−5.43	−25.91	Val135	H-bond
Native ligand	−26.44	0	−7.91	−9.29	Val135 Asp133 Lys85	H-bond

Notes: H-Bond: hydrogen bonding, H Phob: hydrophobicity, Vdw: van der waals interactions, Amino acid: bonding of amino acid, Type of interactions: bonding.

Table 2. Molecular docking data of the synthesized compounds with STAT3 (PDB 6NJS).

Compound	Docking score (kcal/mol)	H-bond	Hydrophobicity	vdW	Amino acid	Interaction type
A21	−17.99	−2.06	−3.76	−18.91	E638	H-bond
A13	−17.5	−2.1	−3.85	−19.72	Y640 E638	Pi-cation H-bond
A20	−16.5	−2.18	−3.91	−18.89	E638	H-bond
A17	−15.8	−2.1	−4.08	−18.94	E638	H-bond
A18	−14.3	−2.15	−4.13	−17.97	M660 K658	H-bond H-bond
A39	−17.68	−4.43	−3.86	−21.28	Y640 E638	Pi-cation H-bond
A40	−16.65	−2.13	−3.43	−19.17	Y640 E638	Pi-cation H-bond
A34	−17.79	−1.95	−3.93	−19.00	E638	H-bond
A31	−17.62	−2.12	−3.98	−19.73	—	—
A33	−16.73	−2.19	−4.10	−19.03	E638	H-bond
A32	−17.10	−1.98	−4.27	−19.37	E638	H-bond
A35	−16.56	−2.16	−3.97	−19.27	Y640 E638	Pi-cation H-bond
A36	−18.62	−1.98	−4.47	−21.22	Y640 E638	Pi-cation H-bond
A72	−13.89	−1.48	−3.64	−22.69	E638 S613	H-bond H-bond
Native ligand	−64.07	−16.99	−6.98	−45.36	Val135 Asp133 Lys85	H-bond H-bond H-bond

Notes: H-bond, hydrogen bond; vdW, van der Waals interactions; interacting residues are shown by their one-letter amino acid code and residue number. A dash (—) indicates no significant interaction detected.

then lysed in ice-cold sodium dodecyl sulfate (SDS) buffer. The lysates were sonicated for thorough homogenization, and protein concentrations were determined using the Pierce protein assay kit according to the manufacturer's instructions. The lysates were aliquoted and stored at −20 °C until use. Protein samples (20 μL per lane) were resolved by 10% polyacrylamide gel electrophoresis and then transferred onto PVDF membranes. Membranes were blocked and incubated with primary antibodies anti-GSK3β (Santa Cruz Biotechnology, Santa Cruz, CA, USA) and anti-phospho-Ser9-GSK3β, followed by horseradish peroxidase-conjugated secondary antibodies. Immunoreactive bands were visualized under a gel doc image analyzer using Genesys software.

Statistical analysis

Statistically significant differences among the various drug treatments were determined using one-way analysis of variance and Student's t-test in Prism 10.0.1 software (GraphPad Inc.). Statistical significance was set at $P < 0.05$.

Results

Network pharmacology

Identification of shared hub targets between indole analogues and Alzheimer's disease

The compound–disease overlap analysis included 14 synthesized indole analogues and an Alzheimer's disease gene set containing more than 1,000 initially retrieved disease-associated genes. The Venn analyses demonstrated identified using Venny v2.1 (https://bioinfogp.cnb.csic.es/tools/venny/). The specific intersections with the AD target set, while the subsequent PPI topology analysis converged on GSK3β, STAT3, MMP2, PARP1, and MAOB as the principal shared hubs.

The integrated protein-protein interaction (PPI) analysis identified a highly connected network comprising 198 nodes and 504 edges for the indole-analogue-associated network and 66 nodes and 198 edges for the disease-specific network. STRING v12 analysis performed at a confidence threshold > 0.9 produced an Alzheimer's disease (AD) network containing 98 nodes and 257 edges and an indole-analogue network containing 166 nodes and 384 edges. The reported average node degree was 2.31 and the local clustering coefficient was 0.339. These values indicate that the networks were not merely collections of isolated targets but contained measurable interconnectivity and local clustering.

CytoHubba analysis using the Maximum Clique Centrality (MCC) algorithm ranked GSK3β as the highest scoring hub in Figure 1A, with an MCC score of 15, followed by STAT3 (MCC = 14), MMP2 (MCC = 7), PARP1 (MCC =

Table 3. Molecular docking data of the synthesized compounds with MMP2 (PDB 7XJO).

Compound	Docking score (kcal/mol)	H bond	Hydrophobicity	vdW	Amino acid	Interaction type
A21	−10.16	−0.89	−5.09	−21.75	F87 Y74	Pi-cation Pi-cation
A13	−10.32	−0.99	−5.04	−19.85	—	—
A20	−10.73	−2.19	−5.41	−15.84	—	—
A17	−11.20	−2.78	−5.75	−19.77	A88	H-bond
A18	−13.77	−2.71	−5.61	−24.42	H85 Y74	H-bond Pi-cation
A39	−8.61	−1.36	−5.12	−21.27	Y74	Pi-cation
A40	−9.62	−0.73	−4.93	−22.78	Y74	Pi-cation
A34	−10.67	−1.45	−5.22	−21.05	F87 Y74	Pi-cation Pi-cation
A31	−9.90	−1.05	−5.31	−21.13	Y74	Pi-cation
A33	−11.9	−2.07	−5.58	−20.87	A88 Y74	H-bond Pi-cation
A32	−12.16	−2.73	−5.78	−20.0	A88 Y74	H-bond Pi-cation
A35	−11.28	−1.71	−5.28	−18.85	A88	H-bond
A36	−11.38	−3.15	−6.13	−20.04	A88 H125	H-bond Pi-cation
A72	−13.67	−2.80	−5.07	−20.91	A88 Y74	H-bond Pi-cation
Native ligand	−2.70	−3.77	−4.43	−16.8	E130 A86	H-bond H-bond

Notes: H-bond, hydrogen bond; vdW, van der Waals interactions; interacting residues are shown by their one-letter amino acid code and residue number. A dash (—) indicates no significant interaction detected.

6) and MAOB (MCC = 6). MAOA also showed an MCC score of 6, indicating that the fifth position was shared at the displayed score level. The subsequent hub scores were BCL2A1 (2), ELANE (1), and GCK (1). Thus, GSK3β exceeded STAT3 by 1 MCC unit and MMP2 by 8 MCC units, demonstrating substantially greater network centrality than the other prioritized targets. The color gradient in Figure 1B is consistent with this ranking, with GSK3β occupying the highest-centrality category. Importantly, the figure reports MCC scores rather than numerical node degree values; therefore, node-degree values should not be inferred from the Figure 1C.

The network analysis therefore reduced the larger disease/compound target space to five experimentally tractable targets, with GSK3B showing the highest MCC score (15) and STAT3 the second-highest score (14). This quantitative separation, together with the biological relevance of GSK3β to tau phosphorylation and neuronal degeneration, provided the basis for prioritizing GSK3β for deeper computational and *in vitro* validation (Figure 2) [39].

Gene ontology and pathway enrichment analyses

GO enrichment analysis showed that the selected targets were associated with biological processes related to cellular catabolism, protein regulation, autophagy, synaptic transmission, cellular localization, responses to oxygen containing compounds, and transport. In the biological-process panel, the displayed fold-enrichment values extended to approximately 17-fold, with regulation of cellular catabolic processes representing the highest enrichment among the plotted terms. Autophagy and processes utilizing autophagic mechanisms were also among the strongly enriched terms, with fold-enriched values of approximately 12–13. In the cellular-component analysis, inclusion body showed the highest enrichment at approximately 32-fold, followed by membrane raft/membrane microdomain-associated terms at approximately 13–14-fold and neuronal-cell-body associated terms at approximately 11-fold. The molecular-function panel showed particularly strong enrichment for cuprous-ion binding, with fold-enrichment values of approximately 130-fold, while lipoprotein-particle binding and protein lipid complex binding were approximately 45–50-fold. Tau-protein binding and amyloid beta binding were also among the prominent disease relevant molecular functions, with fold enrichment values of approximately 30–40-fold. The color scales in Figure 3 correspond to −log10 (FDR), with plotted values extending to approximately 20 for biological processes, 13 for cellular components, and 15 for molecular functions. These quantitative enrichment patterns indicate that the selected hubs are associated with autophagy, synaptic function, protein binding, and cellular stress responses rather than a single isolated biological process.

KEGG analysis is identified multiple pathways relevant to neurodegeneration and Alzheimer's disease. Among the plotted pathways, cholesterol metabolism and mitophagy-animal were the most enriched, with fold enrichment values approximately 20–21 and 20, respectively. Sphingolipid metabolism and the pathway of neurodegeneration–multiple disease also showed substantial enrichment at

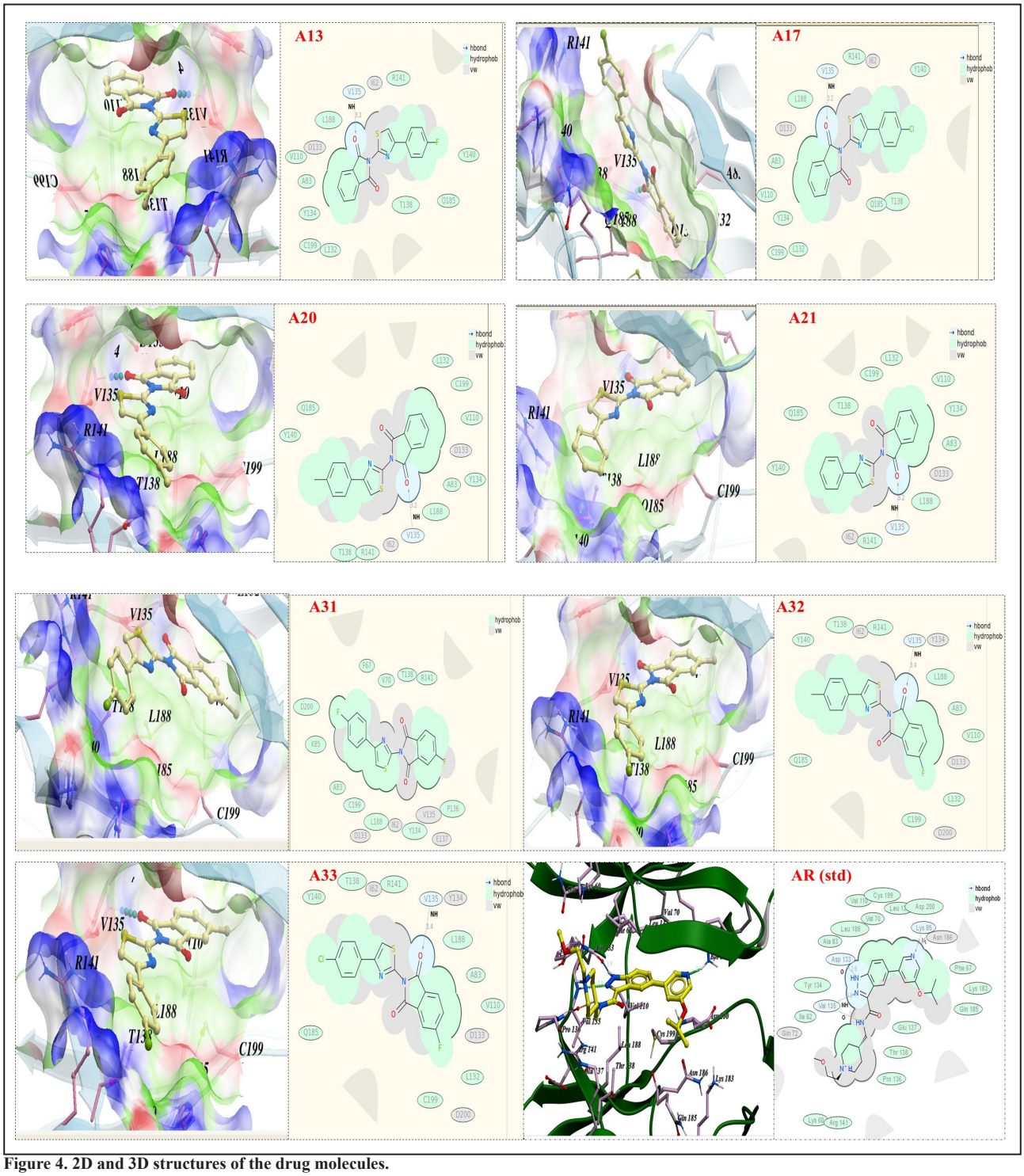

Figure 4. 2D and 3D structures of the drug molecules.

approximately 19 and 18-fold, respectively. Parkinson's disease, amyotrophic lateral sclerosis, osteoclast differentiation, insulin resistance, IL-17 signaling, and Alzheimer's disease were also represented among the enriched pathways, with fold-enrichment values generally ranging from approximately 10 to 16. The Alzheimer's disease pathway itself showed approximately 11-fold enrichment. These results quantitatively support involvement of the selected targets in interconnected processes involving lipid metabolism, mitochondrial function, inflammatory signaling, insulin resistance, and neurodegeneration.

Molecular docking

Molecular docking was performed to screen an in-house compound library, fourteen indole analogues were docked against GSK3β (PDB 6Y9R), STAT3 (PDB 6NJS), and MMP2 (PDB 7XJO), their corresponding chemical structures, names, and molecular weights are summarized in Table 1, Table 2 and Table 3.

GSK3β docking

For GSK3β, docking scores ranged from −16.08 to −24.47, with A36 showing the most favorable score

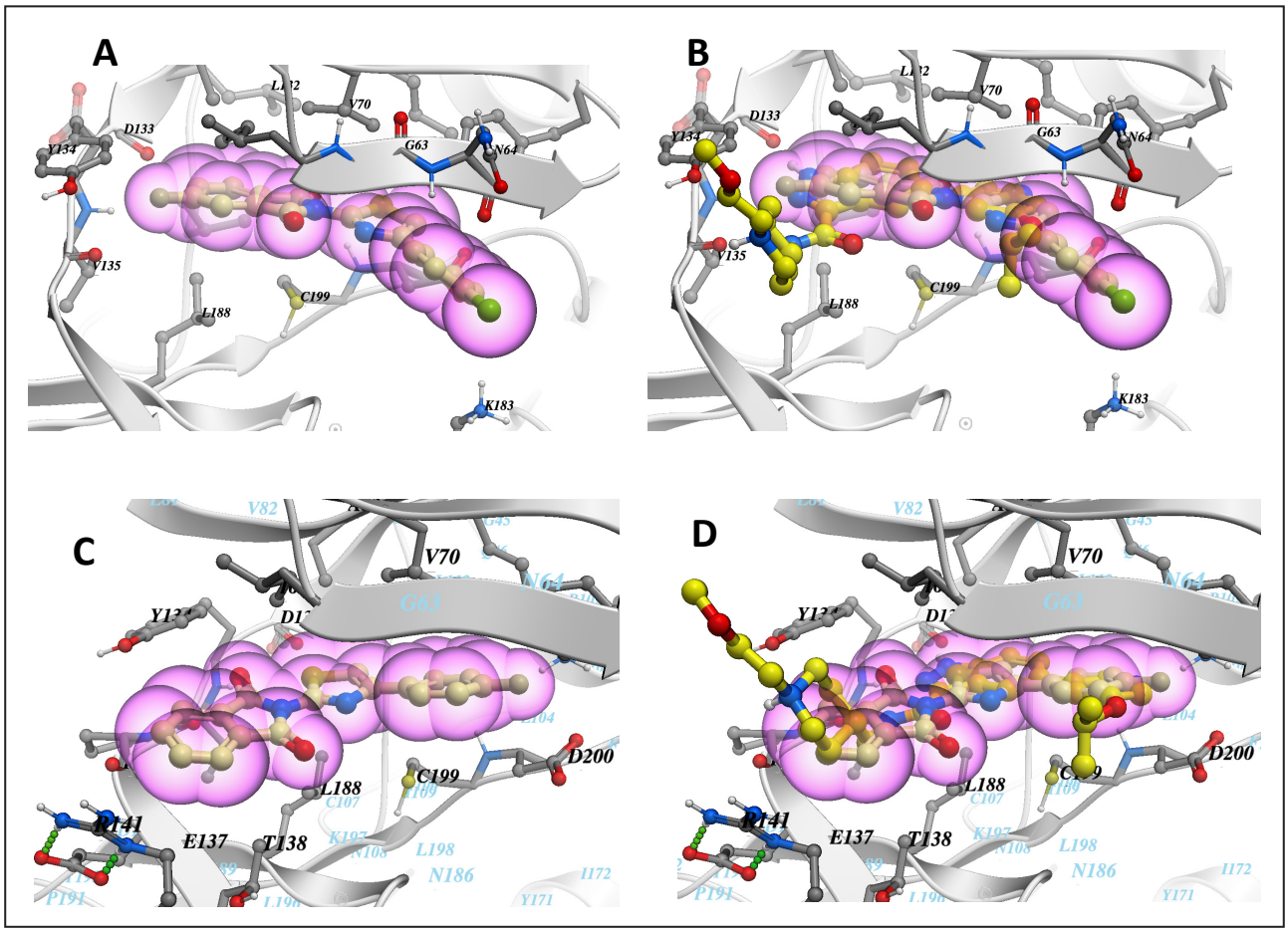

Figure 5. Docking poses of A13 and A33 with GSK3β (PDB 6Y9R). **(A)** Compound A33 docked in 6Y9R; **(B)** Compound A33 with the native ligand of 6Y9R; **(C)** Compound A13 docked in 6Y9R; **(D)** Compound A13 with the native ligand of 6Y9R.

(−24.47), followed by A35 (−23.47), A39 (−23.02), A18 (−22.54), A40 (−20.86), A20 (−20.59), A17 (−20.19), A34 (−19.80), A21 (−18.41), A72 (−18.12), A13 (−18.57), A31 (−17.89), A33 (−16.93), and A32 (−16.08). The native ligand showed a docking score of −26.44 in Table 1.

STAT3 docking

STAT3 docking scores ranged from −13.89 to −18.62 among the 14 analogues. A36 produced the most favorable score (−18.62), followed by A21 (−17.99), A34 (−17.79), A39 (−17.68), A31 (−17.62), A13 (−17.50), A32 (−17.10), A40 (−16.65), A33 (−16.73), A35 (−16.56), A20 (−16.50), A17 (−15.80), A18 (−14.30), and A72 (−13.89). The reported native ligand score was −64.07. Hydrogen-bond interactions involved residues including E638, K658, M660, and S613, while Y640 participated in π-cation interactions for several compounds. The docking data therefore confirmed that the analogues can occupy the STAT3 binding environment, although their docking scores were substantially less favorable than of the native ligand shown in Table 2.

MMP2 docking

MMP2 docking scores ranged from −8.61 to −13.77. A18 showed the most favorable analogue score (−13.77), followed by A72 (−13.67), A33 (−11.90), A36 (−11.38), A35 (−11.28), A17 (−11.20), A20 (−10.73), A34 (−10.67), A13 (−10.32), A21 (−10.16), A31 (−9.90), A40 (−9.62), and A39 (−8.61). The native ligand had a reported score of −2.70. The principal interaction residues included A88, H85, F87, and Y74, with both hydrogen-bond and π-cation interaction observed. Compared with the reported MMP2 native–ligand score, the indole analogues displayed more favorable docking scores, supporting the possibility of productive binding to the selected MMP2 structure as in Table 3.

Compounds A13 and A33 were attached to the ATP-binding pocket of the GSK3β receptor (PDB 6Y9R). The native ligand showed poor binding compared to A13 and A33. The native ligand protruded outside the pocket, whereas A13 and A33 molecules were perfectly bound inside the pocket (Figure 4).

ADME and drug-likeness evaluation

The physicochemical parameters of the synthesized compounds (A13–A72) were evaluated according to Lipinski's rule of five. The 14 compounds showed molecular weights of 306.3–369.3 g/mol, logP values of 3.943–5.295, hydrogen-bond acceptors of 5–9, Zero hydrogen-bond donors, 2–3 rotatable bonds, polar surface areas of 70.62–162.57 Å^2, and drug-likeness scores of −0.70–0.23. A20 had the highest drug-likeness score (0.23), while A72 had the lowest (−0.70). A33 had the highest logP (5.295), followed by A32 (5.124), placing both slightly above the conventional

Table 4. Physicochemical properties and drug-likeness parameters.

Compound	MW (g/mol)	LogS	LogP	HBA	HBD	Rot B	PSA (Å²)	DL
REF	> 500	> −4	≥ 5	≤ 10	≤ 5	≤ 10	< 140	—
A13	324.3	−5.998	4.407	5	0	2	72.10	0.11
A17	320.4	−6.007	4.802	5	0	2	71.56	−0.14
A18	336.4	−5.977	4.361	6	0	3	85.73	−0.10
A20	340.8	−5.573	4.973	5	0	2	70.62	0.23
A21	306.3	−4.966	4.273	5	0	2	70.90	−0.62
A31	342.3	−5.994	4.729	5	0	2	75.70	−0.41
A32	338.4	−6.070	5.124	5	0	2	75.16	−0.28
A33	358.8	−6.131	5.295	5	0	2	74.22	−0.30
A34	324.3	−5.966	4.595	5	0	2	74.50	−0.37
A35	354.4	−6.066	4.683	6	0	3	89.30	−0.19
A36	337.3	−5.021	4.264	6	0	2	115.97	−0.50
A39	319.3	−4.690	3.943	6	0	2	112.37	−0.38
A40	351.3	−5.371	4.304	9	0	3	158.97	−0.61
A72	369.3	−6.072	4.62	9	0	3	162.57	−0.70

Notes: MW, molecular weight; LogS, logarithm of aqueous solubility; LogP, logarithm of octanol–water partition coefficient; HBA, number of hydrogen bond acceptors; HBD, number of hydrogen bond donors; Rot B, number of rotatable bonds; PSA, polar surface area (Å²); DL, drug-likeness score (positive values indicate higher drug-likeness).

Table 5. Predicted permeability and efflux properties of the tested compounds.

Compound	BBB	Caco-2 Log EffluxR	Caco-2 Log PappAB	Caco-2 Log PappBA	Caco-2 Log Papp	MDCK Log EffluxR	MDCK Log PappAB	MDCK Log PappBA	MDCK Log Papp
A13	Yes	0.1890	−4.744	−4.932	−4.703	0.235	−4.664	−4.789	−4.369
A17	Yes	0.3440	−4.976	−5.157	−4.903	0.277	−4.775	−4.972	−4.725
A18	No	0.2865	−4.740	−4.842	−4.807	0.225	−4.845	−4.873	−4.583
A20	Yes	0.1217	−4.820	−4.986	−4.791	0.211	−4.870	−4.933	−4.517
A21	Yes	0.1062	−4.888	−5.090	−4.522	0.291	−4.960	−4.919	−4.433
A31	Yes	0.1229	−4.531	−4.784	−4.703	0.196	−4.250	−4.550	−4.365
A32	Yes	0.2336	−4.713	−4.965	−4.870	0.261	−4.239	−4.588	−4.682
A33	Yes	0.0246	−4.571	−4.846	−4.743	0.178	−4.305	−4.570	−4.471
A34	No	0.1556	−4.811	−5.008	−4.580	0.225	−4.396	−4.633	−4.498
A35	No	0.2270	−4.498	−4.733	−4.711	0.174	−4.525	−4.599	−4.655
A36	No	0.1818	−4.591	−4.764	−4.810	0.195	−4.408	−4.559	−4.694
A39	No	0.2740	−4.857	−4.910	−4.794	0.262	−4.816	−4.806	−4.640
A40	No	0.3646	−4.517	−4.804	−5.066	0.992	−5.009	−4.719	−4.342
A72	No	0.2663	−4.277	−4.689	−5.081	0.684	−4.657	−4.646	−4.420

Notes: BBB, blood–brain barrier; Caco2, human colorectal adenocarcinoma cell line; MDCK, Madin-Darby canine kidney cells; Papp, apparent permeability coefficient (cm/s); EffluxR, efflux ratio (PappBA/PappAB); AB, apical-to-basolateral transport; BA, basolateral-to-apical transport.

logP value of 5.A40 and A72 had the largest PSA values, 158.97 and 162.57 Å^2, respectively varies A20 had the lowest PSA (70.62 Å^2). These values indicate that most compounds remained within the principal physicochemical ranges used for drug likeness assessment, while A40 and A72 may face greater permeability limitations because of their longer polar surface areas as shown in Table 4.

BBB and membrane permeability

Seven compounds (A13, A17, A20, A21, A31, A32 and A33), where predicted to cross the blood–brain barrier, whereas A18, A34, A35, A36, A39, A40, and A72 were predicted to be non-permeable. Caco-2 LogPapp values ranged from −4.277 to 5.081 and Caco-2 efflux ratios from 0.0246 to 0.3646. A33 had the lowest Caco-2 efflux ratio (0.0246), whereas A40 had the highest (0.3646). MDCK log Papp values ranged from −4.342 to −4.725, while MDCK efflux ratios ranged from 0.174 to 0.992. The highest MDCK efflux ratio was observed for A40 (0.992), followed by A72 (0.684), whereas A33 showed the lowest value (0.178). These data identify A13, A20, A31, A32 and A33 as the compounds with the most balanced combination of predicted BBB penetration and per-

Table 6. *In silico* ADMET and toxicity prediction of the synthesized compounds.

Compound	hERG	P-gp	CYP450	McpLD$_{50}$	PAINS
A13	0.200	Yes	CYP1A2: Yes CYP2C19: Yes CYP2C9: No CYP2D6: No CYP3A4: No	logLD$_{50}$PO: 3.15 logLD$_{50}$IV: 2.52 logLD$_{50}$IP: 2.98 logLD$_{50}$SC: 3.34 logLD$_{50}$OTHER: 3.22	0.040588
A17	0.171	Yes	CYP1A2: Yes CYP2C19: Yes CYP2C9: No CYP2D6: No CYP3A4: No	logLD$_{50}$PO: 3.36 logLD$_{50}$IV: 2.75 logLD$_{50}$IP: 2.94 logLD$_{50}$SC: 3.42 logLD$_{50}$OTHER: 3.45	0.045608
A18	0.143	Yes	CYP1A2: Yes CYP2C19: Yes CYP2C9: Yes CYP2D6: No CYP3A4: Yes	logLD$_{50}$PO: 3.14 logLD$_{50}$IV: 2.35 logLD$_{50}$IP: 2.89 logLD$_{50}$SC: 3.38 logLD$_{50}$OTHER: 3.23	0.059601
A20	0.244	Yes	CYP1A2: Yes CYP2C19: Yes CYP2C9: Yes CYP2D6: No CYP3A4: No	logLD$_{50}$PO: 3.2 logLD$_{50}$IV: 2.44 logLD$_{50}$IP: 2.79 logLD$_{50}$SC: 3.35 logLD$_{50}$OTHER: 3.19	0.04796
A21	0.094	Yes	CYP1A2: Yes CYP2C19: Yes CYP2C9: No CYP2D6: No CYP3A4: No	logLD$_{50}$PO: 3.08 logLD$_{50}$IV: 2.52 logLD$_{50}$IP: 2.92 logLD$_{50}$SC: 3.27 logLD$_{50}$OTHER: 3.18	0.033912
A31	0.201	Yes	CYP1A2: Yes CYP2C19: No CYP2C9: No CYP2D6: No CYP3A4: No	logLD$_{50}$PO: 3.17 logLD$_{50}$IV: 2.72 logLD$_{50}$IP: 2.81 logLD$_{50}$SC: 3.28 logLD$_{50}$OTHER: 3.31	0.04009
A32	0.205	Yes	CYP1A2: Yes CYP2C19: Yes CYP2C9: No CYP2D6: No CYP3A4: No	logLD$_{50}$PO: 3.13 logLD$_{50}$IV: 2.4 logLD$_{50}$IP: 2.89 logLD$_{50}$SC: 3.31 logLD$_{50}$OTHER: 3.21	0.058832
A33	0.313	Yes	CYP1A2: Yes CYP2C19: Yes CYP2C9: No CYP2D6: No CYP3A4: No	logLD$_{50}$PO: 3.15 logLD$_{50}$IV: 2.48 logLD$_{50}$IP: 2.79 logLD$_{50}$SC: 3.27 logLD$_{50}$OTHER: 3.16	0.0463
A34	0.159	Yes	CYP1A2: Yes CYP2C19: Yes CYP2C9: No CYP2D6: No CYP3A4: No	logLD$_{50}$PO: 3.09 logLD$_{50}$IV: 2.52 logLD$_{50}$IP: 2.8 logLD$_{50}$SC: 3.24 logLD$_{50}$OTHER: 3.16	0.049024
A35	0.269	Yes	CYP1A2: Yes CYP2C19: Yes CYP2C9: No CYP2D6: No CYP3A4: Yes	logLD$_{50}$PO: 3.16 logLD$_{50}$IV: 2.49 logLD$_{50}$IP: 2.8 logLD$_{50}$SC: 3.31 logLD$_{50}$OTHER: 3.2	0.055587
A36	0.228	Yes	CYP1A2: Yes CYP2C19: No CYP2C9: No CYP2D6: No CYP3A4: No	logLD$_{50}$PO: 3.24 logLD$_{50}$IV: 2.36 logLD$_{50}$IP: 2.81 logLD$_{50}$SC: 3.42 logLD$_{50}$OTHER: 3.26	0.054924
A39	0.144	Yes	CYP1A2: Yes CYP2C19: Yes CYP2C9: No CYP2D6: No CYP3A4: No	logLD$_{50}$PO: 3.2 logLD$_{50}$IV: 2.43 logLD$_{50}$IP: 2.82 logLD$_{50}$SC: 3.33 logLD$_{50}$OTHER: 3.25	0.048203
A40	0.247	Yes	CYP1A2: Yes CYP2C19: No CYP2C9: No CYP2D6: No CYP3A4: No	logLD$_{50}$PO: 3.01 logLD$_{50}$IV: 2.48 logLD$_{50}$IP: 2.69 logLD$_{50}$SC: 3.25 logLD$_{50}$OTHER: 3.24	0.048047

Table 6 continued

Compound	hERG	P-gp	CYP450	McpLD$_{50}$	PAINS
A72	0.325	Yes	CYP1A2: Yes CYP2C19: No CYP2C9: No CYP2D6: No CYP3A4: No	logLD$_{50}$PO: 3.13 logLD$_{50}$IV: 2.45 logLD$_{50}$IP: 2.69 logLD$_{50}$SC: 3.35 logLD$_{50}$OTHER: 3.28	0.058088

Notes: hERG, human ether-à-go-go-related gene (cardiac toxicity risk); P-gp, P-glycoprotein (efflux transporter); CYP450, cytochrome P450 (drug-metabolizing enzyme); LD$_{50}$, median lethal dose; PAINS, pan-assay interference compounds (promiscuous bioactivity risk).

meability characteristics as in Table 5.

Toxicity, PAINS, hERG, P-gp and inflammatory predictions

The predicted hERG scores ranged from 0.094 to 0.325, with A21 showing the lowest value (0.094) and A72 the highest (0.325); all remained below the reported 0.5 threshold used in the manuscript for hERG liability. All 14 compounds were predicted to be P-gp substrates. PAINS score ranged from 0.033912 for A21 to 0.059601 for A18, remaining below the 0.5 threshold for promiscuous/PAINS behavior. The predicted oral LogLD$_{50}$ values ranged from 3.01 for A40 to 3.36 for A17, while the complete route-specific values also remained within the reported low-toxicity prediction range inflammatory prediction scores were all below 0.5. The highest anti-inflammatory Mcp value was observed for A40 (0.282053), followed by A35 (0.093091) and A36 (0.095781) whereas A31 showed a low value of 0.061227. Pro-inflammatory Mcp value were uniformly very low, ranging from 0.00000325 for A33 to 0.000754966 for A13. Collectively, computational toxicity data did not identify major PAINS, hERG, or predicted inflammatory liabilities within the tested series, as shown in Table 6 and Table 7.

MD simulation

A 100-ns molecular- dynamics simulation was performed for GSK3β complexes with A13, A33, and the native ligand, with the final 90 ns used for quantitative analysis. The mean Cα-backbone RMSD was 0.42 ± 0.08 Å for A13, 0.48 ± 0.10Å for A33, and 0.65 ± 0.15Å for the native ligand. Thus, A13 and A33 showed lower mean backbone deviation than the native ligand complex. Mean RMSF values were 1.8 ± 0.6 Å for A13, 1.6 ± 0.5 Å for A33, and 2.9 ± 1.2 Å for the native ligand, indicating reduced average residue flexibility in the analogue-bound systems. The mean radius of gyration was 21.82 ± 0.08 Å for A13, 21.75 ±0.07 Å for A33, and 21.95 ± 0.12 Å for the native ligand, while mean SASA values were 18,850 ± 180, 18,920 ± 160, and 19,350 ± 220 Å², respectively. Total system hydrogen bonds averaged 415 ± 18 for A13, 428 ± 15 for A33, and 418 ± 20 for the native ligand. Ligand-protein hydrogen bonds with > 50% occupancy averaged 2.8 ± 0.4 for A13, 3.2 ± 0.5 for A33, and 2.1 ± 0.6 for the native ligand. The Val135 interaction retained >85% occupancy for both A13 and A33. These values quantitatively support stable complex formation, with A13 showing the lowest RMSD and A33 showing the lowest RMSF and the highest ligand protein hydrogen-bond count among the two analogues as in Table 8.

The A33 trajectory showed RMSD values of approximately 0.05–0.65 Å, RMSF values of approximately 1.5–3.2 Å, radius-of-gyration values of approximately 21.65–21.85 Å , SASA values of approximately 18,700–19,200 Å², and hydrogen-bond counts of approximately 410–445 over the displayed 100-ns trajectory. These ranges indicate that

Table 7. Inflammatory index of the tested compounds.

Compound	Inflammatory Index	Mcp classification	Anti-inflammatory score	Pro-inflammatory score
A13	0.137601	Anti-inflammation	0.137601	0.000754966
A17	0.172672	Anti-inflammation	0.172672	0.0000497667
A18	0.180144	Anti-inflammation	0.180144	0.000262742
A20	0.098531	—	0.098531	0.00003623557
A21	0.160914	Anti-inflammation	0.160914	0.000305009
A31	0.061227	—	0.061227	0.000004976156
A32	0.099215	—	0.099215	0.000005094565
A33	0.062067	—	0.062067	0.000003249292
A34	0.086789	—	0.086789	0.00001048993
A35	0.093091	Anti-inflammation	0.093091	0.00002566321
A36	0.095781	Anti-inflammation	0.095781	0.000007564441
A39	0.121704	Anti-inflammation	0.121704	0.000345323
A40	0.282053	Anti-inflammation	0.282053	0.0001910681
A72	0.110132	Anti-inflammation	0.110132	0.000003418285

Table 8. 100 ns MD simulation parameters for GSK3β (PDB 6Y9R) complexes.

Parameter	A13	A33	Native ligand
Cα backbone RMSD (Å)	0.42 ± 0.08	0.48 ± 0.10	0.65 ± 0.15
RMSF (Å)	1.80 ± 0.60	1.60 ± 0.50	2.90 ± 1.20
Rg (Å)	21.82 ± 0.08	21.75 ± 0.07	21.95 ± 0.12
SASA (Å²)	18,850 ± 180	18,920 ± 160	19,350 ± 220
Total number of H-bonds	415 ± 18	428 ± 15	418 ± 20
Ligand-protein H-bonds (occupancy > 50%)	2.80 ± 0.40	3.20 ± 0.50	2.10 ± 0.60

Notes: MD, molecular dynamics; RMSD, root-mean-square deviation; RMSF, root-mean-square fluctuation; Rg, radius of gyration; SASA, solvent-accessible surface area; H-bonds, hydrogen bonds.

the A33 complex remained within a relatively constrained conformational envelope throughout the simulation. The numerical comparison in Table 8 nevertheless shows that A13 had the lower mean RMSD (0.42 Å versus 0.48 Å), whereas A33 had the lower mean RMSF (1.6 Å versus 1.8 Å) and greater mean ligand-protein hydrogen bonding (3.2 versus 2.8) as in Figure 6 and Figure 7.

MM-GBSA analysis

MM-GBSA analysis showed that the native/standard ligand had the most favorable reported total binding free energy, Gtotal = −11.46 ± 3.4 kcal/mol, Followed by A13 at −8.42 ± 4.2 kcal/mol, whereas A33 had a positive Gtotal of 10.54 ± 5.4 kcal/mol. The EVDW was −29.21 ± 4.2 kcal/mol for the standard, −19.45 ± 3.1 kcal/mol for A13, and −18.82 ± 2.9 kcal/mol for A33. EELE was −221.89 ± 31.1 kcal/mol, −108 ± 19.8 kcal/mol, and −105 ± 16.2 kcal/mol, respectively. Polar solvation (GGB) opposed binding, with values of 192.32 ± 28.6 kcal/mol for the standard, 121 ± 14.5 kcal/mol for A13, and 118 ± 13.6 kcal/mol for A33, whereas the nonpolar solvation term (GSA) remained favorable at −4.81 ± 0.5, −3.83 ± 0.6, and −3.14 ± 0.5 kcal/mol, respectively. The gas-phase contribution (Ggas) was −246.88 ± 29.3 kcal/mol for the standard, −131 ± 24.6 kcal/mol for A13, and −124 ± 22.8 kcal/mol for A33, while Gsolv was 189.32 ± 26.4, 119.42 ±23.1, and 109 ± 21.4 kcal/mol, respectively. Thus, the MM-GBSA analysis did not support A33 as the most energetically favorable complex despite MD trajectory; A13 showed a favorable negative total energy, but its calculated affinity remained weaker than that of the standard ligand Table 9.

MTT assay

N2a cell viability was evaluated over 0.25–30μM. Under normoxic conditions, the IC_{50} values were 6.239 μM for

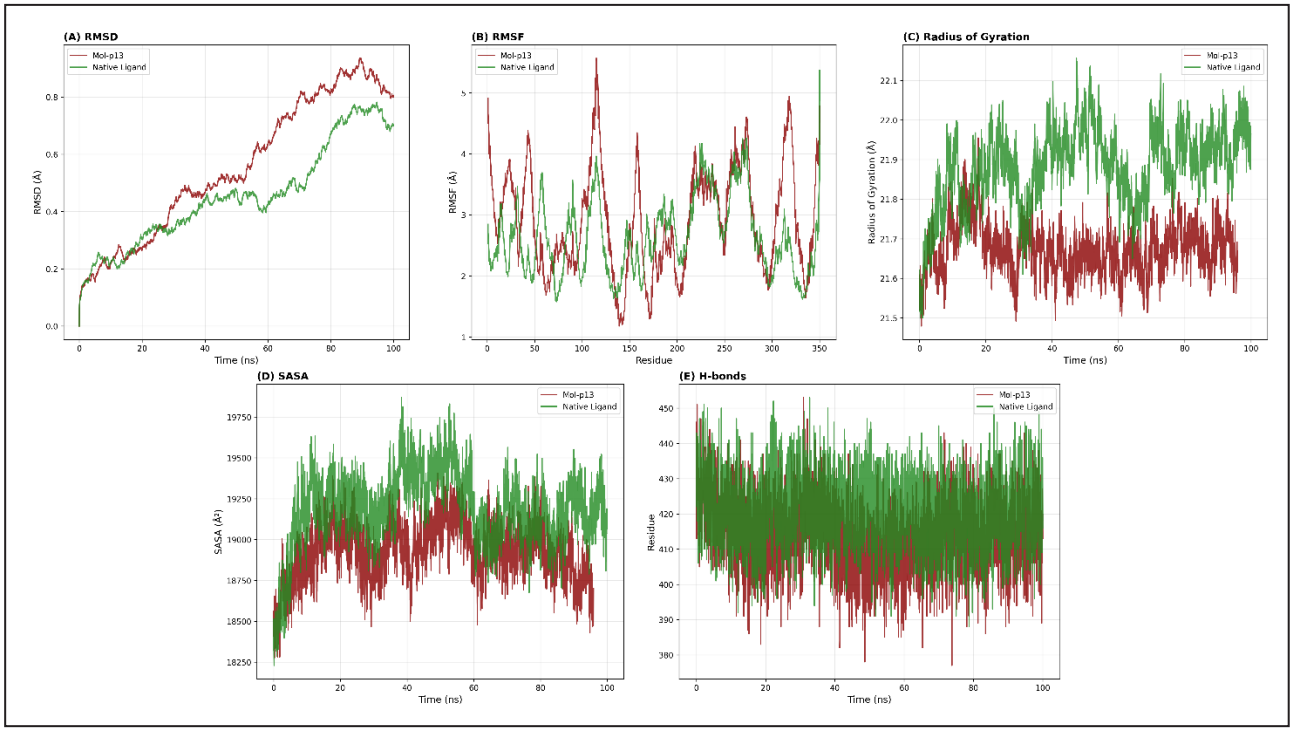

Figure 6. Molecular dynamics analysis of GSK-3β complexes with selected indole analogs. The trajectories correspond to single 100 ns molecular dynamics simulations performed for each protein–ligand complex. Panels (A–D) show the RMSD, RMSF, radius of gyration (Rg), and solvent-accessible surface area (SASA), respectively. The panels include the trajectories of the native ligand and selected indole analogs for comparative analysis.

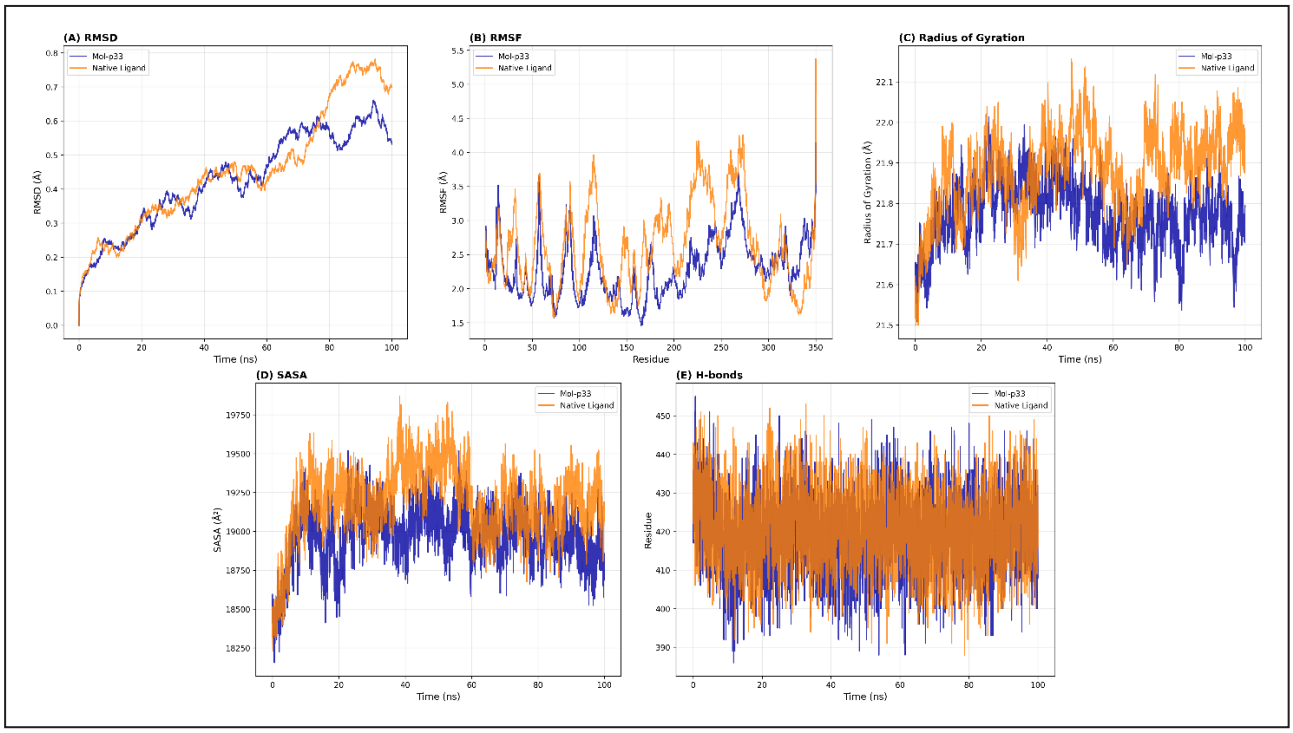

Figure 7. Molecular dynamics (MD) simulation descriptors for the Mol-A33 complex over 100 ns. **(A)** RMSD indicating stable conformational behavior (0.05–0.65 Å). **(B)** RMSF showing reduced flexibility across the functional regions (1.5–3.2 Å). **(C)** Compactness assessment via Rg values (21.65–21.85 Å), suggesting improved folding stability of the peptide. **(D)** SASA analysis demonstrating lower solvent exposure (18,700–19,200 Å^2). (E) Hydrogen bond count (410–445), the highest among the tested ligands. Mol-A13 exhibits superior structural stabilization compared to A33.

A13, 10.64μM for A17, 7.207 μM for A33, 31.45 μM for A34, 185.6 μM for A36, and 9.375 μM for the AR standard. A13 therefore showed the greatest potency among the synthesized analogues under normoxia, with an IC_{50} approximately 1.15-fold lower than A33 and approximately 1.50-fold lower than the AR standard. The dose-response fits were strong, with R^2 values of 0.9964 for A13, 0.9877 for A17, 0.9986 for A33, 0.9957 for A34, 0.9897 for A36, and 0.9681 for the AR standard. The large IC_{50} values of A34 and especially A36 indicate substantially weaker cellular potency under normoxic conditions, as shown in Figure 8A.

Hypoxia-induced cell model

Following 6 h hypoxic exposure and 24 h of compound treatment, IC_{50} values were 7.335 μM for A13, 42.92 μM for A17, 9.571 μM for A33, 29.84 μM for A34, 127.7 μM for A36, and 13.58 μM for the AR standard. A13 again showed the lowest IC_{50} and therefore the highest potency among the synthesized analogues. Relative to normoxia, the IC_{50} of A13 increased from 6.239 to 7.335 μM (approximately 17.6%), whereas A33 increased from 7.207 to 9.571 μM (approximately 32.8%). A17 showed the largest deterioration in apparent potency, increasing from 10.64 to 42.92 μM, approximately fourfold. The reported R^2 values were 0.9967 for A33, 0.9939 for A34, 0.9943 for A36, and 0.9642 for the AR standard, supporting good concentration-response fitting despite the compound-dependent shift in potency in Figure 8B.

Glutamate-induced cytotoxicity (GIC)

In the glutamate-induced neurotoxicity model, the IC_{50} values were 1.8731 μM for A13, 2.1013 μM for A17, 2.2801 μM for A33, 3.1109 μM for A34, 3.0966 μM for

Table 9. MM/GBSA binding free energy components for the reference compound, A13, and A33 complexed with GSK3β.

Energy Component	Standard molecule	A13	A33
EvdW (kcal/mol)	−29.2 ± 4.2	−19.4 ± 3.1	−18.8 ± 2.9
Eele (kcal/mol)	−221.9 ± 31.1	−108.0 ± 19.8	−105.0 ± 16.2
GGB (kcal/mol)	192.3 ± 28.6	121.0 ± 14.5	118.0 ± 13.6
GSA (kcal/mol)	−4.8 ± 0.5	−3.8 ± 0.6	−3.1 ± 0.5
Ggas (kcal/mol)	−246.8 ± 29.3	−131.0 ± 24.6	−124.0 ± 22.8
Gsolv (kcal/mol)	189.3 ± 26.4	119.4 ± 23.1	109.0 ± 21.4
Gtotal (kcal/mol)	−11.4 ± 3.4	−8.4 ± 4.2	+10.5 ± 5.4

Notes: EvdW: van der Waals energy; Eele: electrostatic energy; GGB: polar solvation energy (Generalized Born model); GSA: nonpolar solvation energy (solvent accessible surface area); Ggas: gas-phase energy (EvdW + Eele); Gsolv: solvation energy (GGB + GSA); Gtotal: total binding free energy (Ggas + Gsolv).

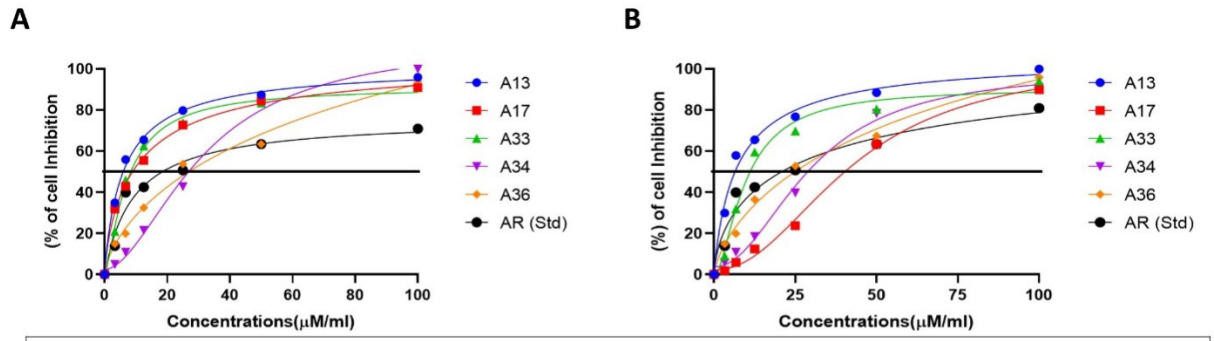

MTT Assay						
Compounds	A13	A17	A33	A34	A36	AR (Std)
IC_{50}	6.239	10.64	7.207	31.45	185.6	9.375
R^2	0.9964	0.9877	0.9986	0.9957	0.9897	0.9681
MTT Assay (Hypoxia Induced Model)						
IC_{50}	7.335	42.92	9.571	29.84	127.7	13.58
R^2	0.9967	0.9857	0.9956	0.9939	0.9943	0.9642

Figure 8. MTT cytotoxicity assay in Neuro2a cells. (A) Dose-response curves under normoxia with IC_{50} (μM): A13 (6.239), A17 (10.64), A33 (7.207), A34 (31.45), A36 (185.6), AR (Std) (9.375). **(B)** Hypoxia-induced model showing IC_{50} (μM): A13 (7.335), A17 (42.92), A33 (9.571), A34 (29.84), A36 (127.7), and AR (standard) (13.58).

A36, and 4.46 μM for the AR standard. A13 was therefore the most potent compound, followed by A17 and A33, and all five synthesized analogues showed lower IC_{50} values than the AR standard. A13 was approximately 57.9% lower than the standard IC_{50}, while A33 was approximately 48.9% lower. The concentration-response fits were strong, with R^2 values of 0.9975 for A13, 0.9983 for A17, 0.9967 for A33, 0.9931 for A34, and 0.9954 for A36. These quantitative results provide the strongest *in vitro* evidence in the manuscript for the neuroprotective potency of A13 and, secondarily, A33 under glutamate induced injury as shown in Figure 9A-B.

Western blotting

Western blot analysis was performed after treatment with A13 and A33 at 1 and 3 μM for 24 h. The blots showed total GSK3β and phosphor-Ser 9-GSK3β at the expected molecular- weight region at approximately 47 kDa. The densitometric plot showed relative phosphor-GSK3β values of approximately 1.0–1.1 across the four treatment conditions, while total GSK3β values were approximately 1.18–1.24 relative units. The direction of the phosphor-Ser9 signal is consistent with increased inhibitory phosphorylation of GSK3β. The Western blot findings consequently provide quantitative-to-semiquantitative mechanistic support for GSK3β inhibition by A13, and A33 as in Figure 9C.

Discussion

Network pharmacology analysis revealed that GSK3β was the best target, and the docking scores confirmed this. Natural inhibitors with low toxicity remain largely unexplored, despite strong evidence that inhibition of GSK3 isoforms can influence the prognosis of several diseases, including neurodegenerative disorders [40, 41]. In this study, we used a combined biochemical and *in silico* strategy to identify a novel drug from a series of indole analogs [42]. Indole analogs are superior according to network pharmacology, which provides a system-level understanding of the complex interactions between compounds, target genes, and signaling pathways, highlighting GSK3β as a central and preferred target in Alzheimer's disease [43]. Construction of the gene–gene interaction network and subsequent GO and pathway enrichment analyses revealed that the identified targets are involved in multiple biological processes, molecular functions, and cellular pathways relevant to disease progression, supporting the biological relevance of the selected targets and their corresponding compounds. Although network pharmacology identified GSK3β, STAT3, and MMP2 as major Alzheimer's disease-associated targets and molecular docking was performed against all three proteins, only GSK3β was subjected to MD simulations and experimental validation. This decision was based on its established role as a central regulator of tau hyperphosphorylation and neuronal degeneration, as well as its favorable docking performance and the availability of validated experimental assays. The STAT3 and MMP2 docking analyses supported the network pharmacology predictions and demonstrated the multi-target binding potential of the synthesized compounds [8, 44].

In silico drug discovery approaches further supported the

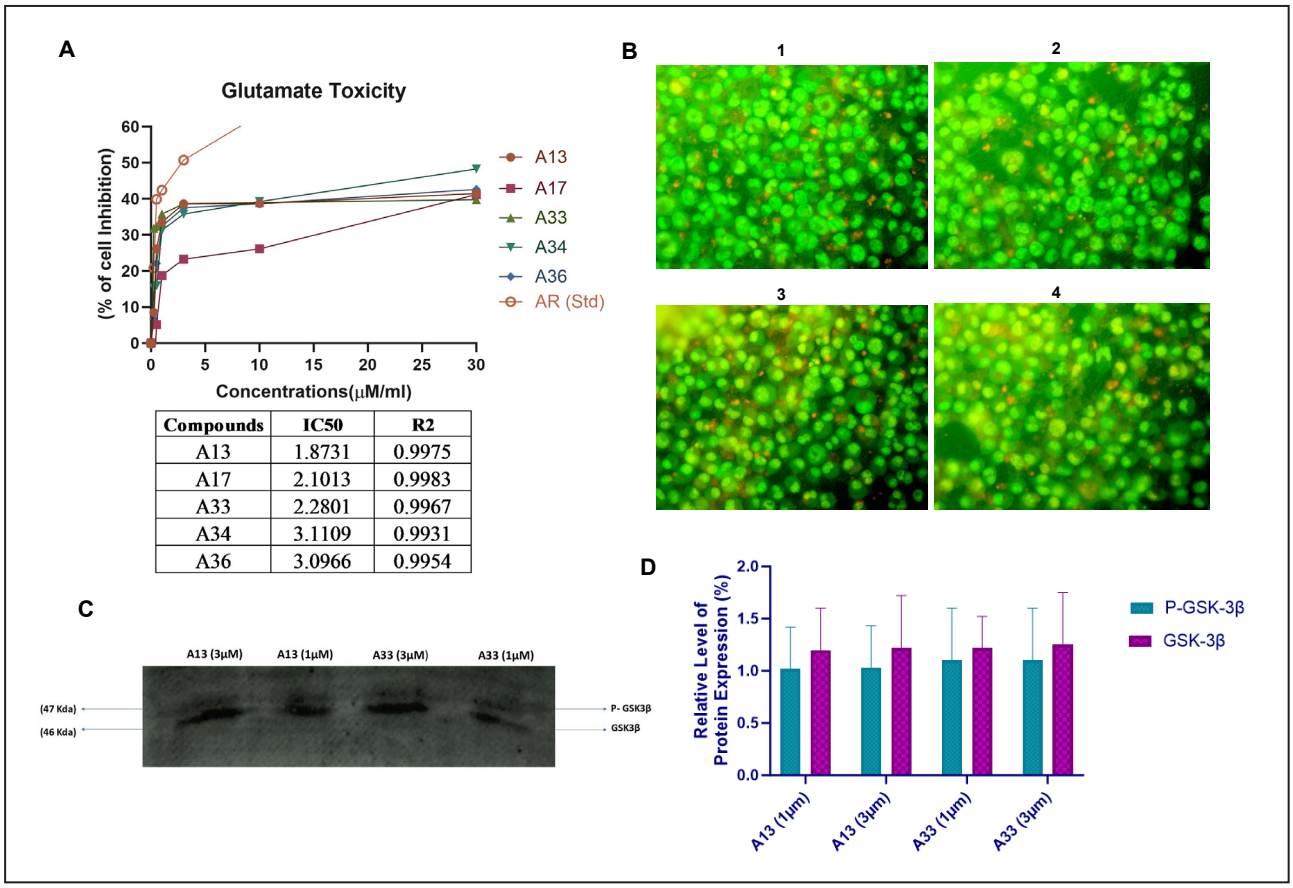

Compounds	IC50	R2
A13	1.8731	0.9975
A17	2.1013	0.9983
A33	2.2801	0.9967
A34	3.1109	0.9931
A36	3.0966	0.9954

Figure 9. Neuroprotective effects of selected indole analogs and their modulation of GSK3β phosphorylation. **(A)** Glutamate Toxicity model showing IC_{50} (µM): A13 (1.87), A17 (2.10), A33 (2.28), A34 (3.11), A36 (3.09), AR (Std) (4.46). **(B)** Representative image of N2a cells exposed to A13 and A33 at two different concentrations. (1) A13 with a 1µM concentration, (2) A13 with a 3 µM concentration, (3) A33 with a 1µM concentration, (4) A33 with a 3µM concentration. **(C)** Western Blot analysis of the above cell lysates was performed; the blots were probed with antibodies against phosphor-GSK3β and total GSK3β. **(D)** Densitometric quantification using the mean of the sum of the ratios of total and phosphor-GSK3β for all samples.

therapeutic potential of the 14 in-house synthesized indole analogs for GSK3β compared with STAT3 and MMP2, as per the docking results in Tables 1-3. Since GSK3β exhibited the highest activity, further screening with ADMET profiling (Table 4-5) demonstrated that most compounds complied with Lipinski's rule of five, indicating favorable drug-like properties [45]. All compounds had molecular weights below 500 Da and log *P* values between 3.9 and 5.2, suggesting an optimal balance between hydrophilicity and lipophilicity, which is important for gastrointestinal absorption, bioavailability, and central nervous system (CNS) penetration. The predicted solubility values (−4.6 to −6.1) indicate slight solubility, which is acceptable for many orally active drugs. The hydrogen bond donors and acceptors across all compounds were within acceptable limits, further confirming their drug-like properties. The polar surface area, a key determinant of intestinal permeability, was within the favorable range for most compounds, except A40 and A72, which showed higher PSA values that may limit their permeability.

MD simulations provide insights into the stability of ligand–protein complexes. The ligand–protein interactions were stabilized by hydrogen bonding, with the protein backbone and ligand showing increased fluctuations after 80–100 ns but remaining within acceptable limits (0.6 Å for the protein backbone and 2.2 Å for the ligand over the final 100 ns).Notably, Val135 formed a stable hydrogen bond interaction, and interaction analyses of the 6Y9R–A13 and 6Y9R–A33 complexes confirmed persistent contacts throughout the simulation, supporting the reliability of the docking predictions.

While molecular docking was performed on all three network pharmacology-derived targets (GSK3β, STAT3, and MMP2), downstream ADMET profiling, MD simulations, and *in vitro* validation were focused exclusively on GSK3β for the following reasons: (1) GSK3β demonstrated the highest docking scores for the majority of compounds and the deepest engagement with the ATP-binding site via Val135 hydrogen bonding; (2) structural analysis described above confirmed that the indole scaffold lacks the bulky, flexible pharmacophoric elements required for effective STAT3 protein-protein interface inhibition and also lacks the zinc-chelating groups (hydroxamate, carboxylate, or thiol) essential for MMP2 active site binding; and (3) concentrating all experimental resources on the primary target enabled more rigorous mechanistic validation (MD and western blot) rather than superficial coverage of all three targets.

Molecules A13 and A33 bind better to GSK3β because it has an ATP-binding pocket with a narrow hydrophobic

cavity and a hinge region for H-bonding, where imide carbonyl and heterocyclic nitrogen can form strong hydrogen bonds with Val135 and ASP133.However, the interaction with STAT3 is weaker because it is too small and rigid for the STAT3 protein-protein interface, and there is no phosphotyrosine mimic because STAT3 binding pockets require bulky or flexible inhibitors.MMP2 also showed weaker binding because it binds to zinc-binding groups, such as hydroxamate, carboxylate, and thiol, which are strong zinc-chelating groups that are lacking in the drug molecules. Overall, the thiazole-like and indole groups are more likely to bind to kinase than MMP2 and STAT3. Docking and MD results indicated that A13 and A33 formed stable interactions with the ATP-binding pocket of GSK3β. These findings provide structural support for plausible GSK3β-targeted activity, rather than definitive target engagement [46]. Potent GSK3β inhibitors act as ATP-competitive kinase inhibitors. The indole ring mimics adenine-like heteroaromatic systems, allowing strong binding to the ATP pocket. Indole is planar and aromatic, and fits well into the kinase hinge region. The nitrogen of indole forms a hydrogen bond similar to that of ATP's adenine, and the π electrons enable π–π stacking with the aromatic residues phenylalanine and tyrosine. Structure-activity relationship (SAR) studies of indole-based GSK3β inhibitors show that specific substitution on the indole ring increases its inhibition by direct binding interactions with active site residues [47].

Notably, A34, predicted by *in silico* tools to be BBB-impermeable (Table 5), exhibited a moderate IC_{50} of 3.11 µM in the glutamate-induced cytotoxicity model. The *in vitro* experiment was carried out in N2a neuroblastoma cells in standard culture, which do not replicate the tight junctions and efflux transporter activity of the *in vivo* BBB and can account for this apparent disparity. Therefore, rather than reflecting CNS bioavailability *in vivo*, the *in vitro* IC_{50} values for BBB-impermeable drugs represent the direct cytosolic activity in a permeable cell model. Although A34 exhibits modest *in vitro* efficacy, A13 and A33 (both BBB-permeable) are prioritized as leads for drug development because BBB permeability is a crucial selection criterion.

Biological validation using the MTT assay and hypoxia cell model in N2a cells demonstrated that the indole analogs exerted comparable effects on cell viability, either by inducing cell death or inhibiting proliferation [48]. The MTT assay measures mitochondrial dehydrogenase activity as a surrogate for cell viability, although it is not a target-specific assay. Among all the tested compounds, A13 emerged as the most potent, particularly considering their predicted BBB permeability. A13 compound exhibited IC_{50} values of MTT analysis 6.2 µg/mL, and hypoxic cell model 7.3 µg/mL, respectively, indicating substantial cellular survival even at higher concentrations, which may reflect a balance between efficacy and reduced cytotoxicity [49, 50]. Western blot analysis demonstrated that treatment with A13 increased the inhibitory phosphorylation of GSK3β at Ser9, providing supportive evidence for the modulation of the GSK3β signaling pathway. However, this observation represents an association between A13 treatment and GSK3β phosphorylation and should not be interpreted as definitive evidence of direct target-specific inhibition. The neuroprotective effects observed in the MTT assay primarily reflect the preservation of cellular metabolic activity and viability under toxic conditions; therefore, they do not independently establish the molecular mechanism of action. Overall, the integration of network pharmacology, ADMET prediction, molecular docking, MD simulation, and *in vitro* validation strongly supports A13 as promising lead compound targeting GSK3β, with potential for further development as low-toxicity therapeutic candidates for Alzheimer's disease [51].

Conclusions

This study successfully identified novel indole-based GSK3β inhibitors using an integrated strategy that combined network pharmacology, *in silico* modeling, and *in vitro* validation. Network analysis confirmed GSK3β as a key hub target in Alzheimer's disease, while docking against GSK3β, STAT3, and MMP2 supported the multi-target binding potential of the synthesized indole analogs; however, only GSK3β was advanced to MD simulation and experimental validation. ADMET profiling revealed that most compounds exhibit favorable drug-like and CNS-penetrating properties. Biological validation using the MTT assay and a hypoxia cell model identified A13 as the most potent compound in terms of cell-based neuroprotective activity; however, only A13 showed a favorable (negative) MM-GBSA binding free energy, whereas A33's positive value (+10.54 ± 5.4 kcal/mol) indicates thermodynamically unfavorable binding to GSK3β. A13 is therefore regarded as the primary lead compound and A33 as a secondary candidate requiring further mechanistic validation. The IC_{50} values for the glutamate toxicity model for A13 and A33 were 1.87 µM and 2.28 µM, respectively, indicating the neuroprotective effect of the drugs making A13 potent drug. Western blotting confirmed that A13 and A33 increased GSK3β phosphorylation at Ser9, the canonical inhibitory phosphorylation site. Although this is consistent with GSK3β inhibition as the mechanism of neuroprotection, establishing formal causation would require additional investigations, such as pharmacological rescue with a structurally distinct GSK3β inhibitor, CRISPR-mediated gene disruption, and GSK3β-selective knockdown using siRNA. The present findings identify A13 as a promising lead compound with significant neuroprotective activity and supportive evidence for the modulation of the GSK3β signaling pathway. Further mechanistic investigations are required to establish a direct causal relationship between A13 and GSK3β inhibition and to validate its therapeutic potential in appropriate cell models.

Declarations

Acknowledgment: I am thankful to the Tamil Nadu Dr.

M.G.R Medical University, Chennai, for supporting me in my PhD work.

Author contribution: M. Ramanathan: conceptualization, investigation, methodology, formal analysis, validation, writing original draft. G. Manas Kumar: resources, investigation, methodology, and typing. Maida Engels SE: investigation, methodology, formal analysis, validation. Sardar Shamshair Singh performed the investigation, methodology, formal analysis, and validation of *in silico* data. All authors have discussed the results and contributed to writing and editing the final manuscript.

Availability of data and materials: All source data for this study (or generated in this study) are available upon reasonable request.

Financial support and sponsorship: None.

Conflicts of interest: Not applicable.

Ethics approval and consent to participate: Not applicable.

Consent for publication: Not applicable.

AI and AI-assisted tools statement: No AI tools were used in the preparation of this article.

References

1. Yu H, Xiong M, & Zhang Z. The role of glycogen synthase kinase 3 beta in neurodegenerative diseases. *Front Mol Neurosci*, 2023, 16: 1209703. [Crossref]
2. Zhao Z, Yuan Y, Li S, Wang X, & Yang X. Natural compounds from herbs and nutraceuticals as glycogen synthase kinase-3β inhibitors in Alzheimer's disease treatment. *CNS Neurosci Ther*, 2024, 30(8): e14885. [Crossref]
3. Azmal M, Paul J, Talukder O, Been Haque A, & Ghosh A. Computational identification of phytochemicals as glycogen synthase kinase 3 beta (GSK3β) inhibitors for therapeutic applications in chronic diseases. *Sci Rep*, 2025, 15(1): 34882. [Crossref]
4. Eskandarzadeh M, Kordestani-Moghadam P, Pourmand S, Khalili Fard J, Almassian B, & Gharaghani S. Inhibition of GSK_3β by iridoid glycosides of snowberry (Symphoricarpos albus) effective in the treatment of Alzheimer's disease using computational drug design methods. *Front Chem*, 2021, 9: 709932. [Crossref]
5. Shri S, Manandhar S, Nayak Y, & Pai K. Role of GSK-3β inhibitors: new promises and opportunities for Alzheimer's disease. *Adv Pharm Bull*, 2023, 13(4): 688-700. [Crossref]
6. Mehla J, Singh I, Diwan D, Nelson J, Lawrence M, Lee E, *et al*. STAT3 inhibitor mitigates cerebral amyloid angiopathy and parenchymal amyloid plaques while improving cognitive functions and brain networks. *Acta Neuropathol Commun*, 2021, 9(1): 193. [Crossref]
7. Choi H, Cha S, Lee J, Kim H, & Kim K. Recent advances on the role of GSK3β in the pathogenesis of amyotrophic lateral sclerosis. *Brain Sci*, 2020, 10(10): 675. [Crossref]
8. Joshi N, & Alavala R. Identification of novel ligands against GSK-3β: Molecular docking, ADMET filtering, MD simulations, MM-GBSA studies, and DFT analysis. *Comput Biol Chem*, 2025, 118: 108478. [Crossref]
9. Zhang Y, Lv S, Huang P, Xiao L, Lin N, & Huang E. Network pharmacology study on the mechanism of berberine in Alzheimer's disease model. *npj Sci Food*, 2025, 9(1): 16. [Crossref]
10. Puri V, Kanojia N, Sharma A, Huanbutta K, Dheer D, & Sangnim T. Natural product-based pharmacological studies for neurological disorders. *Front Pharmacol*, 2022, 13: 1011740. [Crossref]
11. Durmanova V, Javor J, Parnicka Z, Minarik G, Ocenasova A, Vaseckova B, *et al*. Impact of MMP2 rs243865 and MMP3 rs3025058 Polymorphisms on Clinical Findings in Alzheimer's Disease Patients. *Mediators Inflamm*, 2021, 2021: 5573642. [Crossref]
12. Cantero-Fortiz Y, Butler C, Montalbán X, & Boada M. Cellular senescence in brain aging and neurodegeneration: from molecular mechanisms to translational opportunities. *Front Cell Neurosci*, 2026, 20: 1805691. [Crossref]
13. Ciccone L, Vandooren J, Nencetti S, & Orlandini E. Natural marine and terrestrial compounds as modulators of matrix metalloproteinases-2 (MMP-2) and MMP-9 in Alzheimer's disease. *Pharmaceuticals*, 2021, 14(2): 86. [Crossref]
14. Radosinska D, & Radosinska J. The link between matrix metalloproteinases and Alzheimer's disease pathophysiology. *Mol Neurobiol*, 2025, 62(1): 885-899. [Crossref]
15. Breznik M, Ge Y, Bluck J, Briem H, Hahn D, Christ C, *et al*. Prioritizing small sets of molecules for synthesis through in-silico tools: a comparison of common ranking methods. *ChemMedChem*, 2023, 18(1): e202200425. [Crossref]
16. Ghasemi Tigan M, Ghahghaei A, & Lagzian M. In-vitro and in-silico investigation of protective mechanisms of crocin against E46K α-synuclein amyloid formation. *Mol Biol Rep*, 2019, 46(4): 4279-4292. [Crossref]
17. Bhanwala N, Katiyar R, Kumar S, Datusalia A, & Khatik G. Network pharmacology and in silico investigation into the therapeutic potential of phytoconstituents of Peucedanum ostruthium as anti-tubercular agents. *Health Sci Rev*, 2025, 14: 100219. [Crossref]
18. Mazri R, Ouassaf M, Zekri A, Khan S, Rengasamy K, & Alhatlani B. In silico network pharmacology, molecular docking, and molecular dynamics analysis of rosemary-derived compounds as potential HSP90 inhibitors for cancer therapy. *Curr Issues Mol Biol*, 2025, 47(10): 860. [Crossref]
19. Ram S, More-Adate P, Tagalpallewar A, Pawar A, Nagar S, & Baheti A. An in-silico investigation and network pharmacology based approach to explore the anti-breast-cancer potential of Tecteria coadunata (Wall.) C. Chr. *J Biomol Struct Dyn*, 2024, 42(18): 9650-9661. [Crossref]
20. Kumar S, Abbas F, Ali I, Gupta M, Kumar S, Garg M, *et al*. Integrated network pharmacology and in-silico approaches to decipher the pharmacological mechanism of Selaginella tamariscina in the treatment of non-small cell lung cancer. *Phytomedicine Plus*, 2023, 3(2): 100419.

[Crossref]
21. Zeng P, Fang M, Zhao H, & Guo J. A network pharmacology approach to uncover the key ingredients in Ginkgo Folium and their anti-Alzheimer's disease mechanisms. *Aging*, 2021, 13(14): 18993-19012. [Crossref]
22. Bouone Y, Bouzina A, & Aouf N. Synthesis, molecular docking analysis, ADMET and drug likeness prediction of a benzenesulfonamide derivative analogue of SLC-0111. *Med Sci Forum*, 2022, 14(1): 24. [Crossref]
23. Rajamohamed R, & Veerappapillai S. Identification of novel dihydroorotate dehydrogenase (DHODH) inhibitors for cancer: computational drug repurposing strategy. *BMC Pharmacol Toxicol*, 2025, 26(1): 168. [Crossref]
24. Shaw S, Dey R, Yadav R, Chaube U, Dhameliya T, Vyas V, *et al*. In search of PI3K inhibitors as anticancer agents: molecular modelling through virtual screening, ADMET, and molecular dynamics simulations. *ChemistrySelect*, 2025, 10(36): e00406. [Crossref]
25. Ajala A, Uzairu A, Shallangwa G, & Abechi S. Virtual screening, molecular docking simulation and ADMET prediction of some selected natural products as potential inhibitors of NLRP3 inflammasomes as drug candidates for Alzheimer disease. Biocatal. *Agric Biotechnol*, 2023, 48: 102615. [Crossref]
26. Pandya V, Rao P, Prajapati J, Rawal R, & Goswami D. Pinpointing top inhibitors for GSK3β from pool of indirubin derivatives using rigorous computational workflow and their validation using molecular dynamics (MD) simulations. *Sci Rep*, 2024, 14(1): 49. [Crossref]
27. Ononamadu C, & Ibrahim A. Molecular docking and prediction of ADME/drug-likeness properties of potentially active antidiabetic compounds isolated from aqueous-methanol extracts of Gymnema sylvestre and Combretum micranthum. *BioTechnologia*, 2021, 102(1): 85-99. [Crossref]
28. Phillips J, Hardy D, Maia J, Stone J, Ribeiro J, Bernardi R, *et al*. Scalable molecular dynamics on CPU and GPU architectures with NAMD. *J Chem Phys*, 2020, 153(4): 044130. [Crossref]
29. Leal L, de Sena M, Invenção M, de Moura I, Jesus A, de Sousa G, *et al.* Development and immunogenicity assessment of a multi-epitope antigen against Zika virus: an in silico and in vivo approach. *Vaccines*, 2025, 14(1): 31. [Crossref]
30. Rajpoot V, Karthikeyan C, Subash P, & Rao K. Antiplasmodial metabolites from Baccharoides anthelmintica seeds: in vitro and in silico profiling. *J Ethnopharmacol*, 2026, 355(Pt A): 120661. [Crossref]
31. Thandivel S, Rajan P, Gunasekar T, Arjunan A, Khute S, Kareti S, *et al*. In silico molecular docking and dynamic simulation of anti-cholinesterase compounds from the extract of Catunaregam spinosa for possible treatment of Alzheimer's disease. *Heliyon*, 2024, 10(7): e27880. [Crossref]
32. Saravanan K, Elancheran R, Divakar S, Anand S, Ramanathan M, Kotoky J, *et al*. Design, synthesis and biological evaluation of 2-(4-phenylthiazol-2-yl) isoindoline-1,3-dione derivatives as anti-prostate cancer agents. *Bioorg Med Chem Lett*, 2017, 27(5): 1199-1204. [Crossref]
33. Lauretti E, Dincer O, & Praticò D. Glycogen synthase kinase-3 signaling in Alzheimer's disease. *Biochim Biophys Acta Mol Cell Res*, 2020, 1867(5): 118664. [Crossref]
34. Chen Y, Chen J, Zhao L, Zhang X, Wu X, Wang X, *et al*. Ethyl pyruvate attenuates cerebral hypoxia/reoxygenation injury in neuroblastoma cells: role of GAS6/Axl signaling. *Heliyon*, 2023, 9(12): e22787. [Crossref]
35. Di Mattia M, Mauro A, Citeroni MR, Dufrusine B, Peserico A, Russo V, *et al*. Insight into hypoxia stemness control. *Cells*, 2021, 10(8): 2161. [Crossref]
36. Praisthy L, Kushwah R, Dubey S, Labhade S, Karwa P, & Jain S. Daidzein targets PI3K-Akt signaling and oxidative stress in glioblastoma: an Integrated pharmacological and in vitro study. *Brain Res*, 2025, 1863: 149840. [Crossref]
37. Yuan Y, Tan H, Chen H, Zhang J, Shi F, Wang M, *et al*. Peroxiredoxin 1 alleviates oxygen-glucose deprivation/ reoxygenation injury in N2a cells via suppressing the JNK/ caspase-3 pathway. *Iran J Basic Med Sci*, 2023, 26(11): 1305-1312. [Crossref]
38. Xin H, Cui Y, An Z, Yang Q, Zou X, & Yu N. Attenuated glutamate induced ROS production by antioxidative compounds in neural cell lines. *RSC Adv*, 2019, 9(60): 34735-34743. [Crossref]
39. Naffaa M. Monoamine Oxidase B in Astrocytic Gaba Synthesis: a central mechanism in neurodegeneration and neuroinflammation. *J Cell Signal*, 2025, 6(2): 53-70. [Crossref]
40. Hajka D, Budziak B, Pietras Ł, Duda P, McCubrey J, & Gizak A. GSK3 as a regulator of cytoskeleton architecture: consequences for health and disease. *Cells*, 2021, 10(8): 2092. [Crossref]
41. Arciniegas Ruiz S, & Eldar-Finkelman H. Glycogen synthase Kinase-3 inhibitors: preclinical and clinical focus on CNS-A decade onward. *Front Mol Neurosci*, 2022, 14: 792364. [Crossref]
42. Kumar H, Datusalia A, Kumar A, & Khatik G. Network pharmacology exploring the mechanistic role of indirubin phytoconstituent from Indigo naturalis targeting GSK-3β in Alzheimer's disease. *J Biomol Struct Dyn*, 2025, 43(18): 10959-10972. [Crossref]
43. Balasubramaniam M, Mainali N, Bowroju S, Atluri P, Penthala N, Ayyadevera S, *et al*. Structural modeling of GSK3β implicates the inactive (DFG-out) conformation as the target bound by TDZD analogs. *Sci Rep*, 2020, 10(1): 18326. [Crossref]
44. Delvecchio B, Cicco L, Paparella A, Di Salvo G, Perna F, & Capriati V. A scalable and sustainable synthesis of indirubin frameworks enabled by deep eutectic solvents. *ChemSusChem*, 2026, 19(1): e202502114. [Crossref]
45. Istrate D, & Crisan L. Natural compounds as DPP-4 inhibitors: 3D-similarity search, adme toxicity, and molecular docking approaches. *Symmetry*, 2022, 14(9): 1842. [Crossref]
46. Rajamani G, Naqvi S, & Sharma A. Structure-activity relationship of GSK-3β inhibitors: insight into drug design for Alzheimer's disease. *RSC Med Chem*, 2025, 17(1): 15-51. [Crossref]
47. Vignaux P, Minerali E, Foil D, Puhl A, & Ekins S. Machine

learning for discovery of GSK3β Iinhibitors. *ACS Omega*, 2020, 5(41): 26551-26561. [Crossref]

48. Jin L, Wang Q, Yang M, Zhang J, Liang H, Tan H, *et al*. Indirubin-3′-monoxime-loaded PLGA-PEG nanoparticles for potential Alzheimer's disease treatment. *Med Nov Technol Devices*, 2022, 15: 100150. [Crossref]
49. Magham S, Shanavas S, Pindiprolu S, Nagappan K, More S, Chaudhury D, *et al*. Targeting GSK-3β to modulate the Wnt pathway: a promising neuroprotective strategy for Alzheimer's disease. *Mol Pharm*, 2025, 22(11): 6561-6574. [Crossref]
50. Dan N, Quang H, Van Truong V, Huu Nghi D, Cuong N, Cuong T, *et al*. Design, synthesis, structure, in vitro cytotoxic activity evaluation and docking studies on target enzyme GSK-3β of new indirubin-3'-oxime derivatives. *Sci Rep*, 2020, 10(1): 11429. [Crossref]
51. Zhao J, Wei M, Guo M, Wang M, Niu H, Xu T, *et al*. GSK3: a potential target and pending issues for treatment of Alzheimer's disease. *CNS Neurosci Ther*, 2024, 30(7): e14818. [Crossref]

Cite this article as: Gedla MK, & Muthiah R. Deciphering the action of indole analogues on selected targets for neuroprotection in Alzheimer's disease: network pharmacology, *in silico*, and *in vitro* approaches. *Aging Pathobiol Ther*, 2026, 8(3): xx-xx. doi: 10.31491/APT.2026.09.xxx